2011

A Deep Spectroscopic Study of the Filamentary Nebulosity in NGC 4696, the Brightest Cluster Galaxy in the Centaurus Cluster

R. E. A. Canning
University of Cambridge, UK

A. C. Fabian
University of Cambridge, UK

R. M. Johnstone
University of Cambridge, UK

J. S. Sanders
University of Cambridge, UK

C. S. Crawford
University of Cambridge, UK

See next page for additional authors

Monthly Notices
of the
ROYAL ASTRONOMICAL SOCIETY

Mon. Not. R. Astron. Soc. **417,** 3080–3099 (2011) doi:10.1111/j.1365-2966.2011.19470.x

A deep spectroscopic study of the filamentary nebulosity in NGC 4696, the brightest cluster galaxy in the Centaurus cluster

R. E. A. Canning,[1⋆] A. C. Fabian,[1] R. M. Johnstone,[1] J. S. Sanders,[1] C. S. Crawford,[1] G. J. Ferland[2] and N. A. Hatch[3]

[1]*Institute of Astronomy, University of Cambridge, Madingley Road, Cambridge CB3 0HA*
[2]*Department of Physics, University of Kentucky, Lexington, KY 40506, USA*
[3]*School of Physics & Astronomy, University of Nottingham, Nottingham NG7 2RD*

Accepted 2011 July 18. Received 2011 July 9; in original form 2011 April 21

ABSTRACT

We present results of deep integral-field spectroscopy observations using high-resolution optical (4150–7200 Å) VLT VIsible MultiObject Spectrograph spectra of NGC 4696, the dominant galaxy in the Centaurus cluster (Abell 3526). After the Virgo cluster, this is the second nearest ($z = 0.0104$) example of a cool-core cluster. NGC 4696 is surrounded by a vast, luminous Hα emission-line nebula ($L_{\mathrm{H}\alpha} = 2.2 \times 10^{40}$ erg s^{-1}). We explore the origin and excitation of the emission-line filaments and find their origin consistent with being drawn out, under rising radio bubbles, into the intracluster medium as in other similar systems. Contrary to previous observations, we do not observe evidence for shock excitation of the outer filaments. Our optical spectra are consistent with the recent particle heating excitation mechanism of Ferland et al.

Key words: galaxies: clusters: individual: Centaurus – galaxies: individual: NGC 4696.

1 INTRODUCTION

In this paper, we report on deep (∼12 h) integral-field spectroscopy observations of the extended optical emission-line system surrounding NGC 4696, the brightest cluster galaxy (BCG) in the Centaurus cluster (Abell 3526), which, at a redshift of $z = 0.0104$, is the second nearest example of a 'cool-core' cluster.

Nearly half of all galaxy clusters have dense cores of cool X-ray-emitting gas observed as a sharp peak in their X-ray surface brightness profiles. These 'cool-core' clusters have short cooling times and central temperatures which drop to about a third of the cluster ambient temperature (for a review, see Peterson & Fabian 2006; McNamara & Nulsen 2007). In addition to the sharply peaked X-ray surface brightness profiles, many cool-core clusters have extended filamentary optical emission-line systems around their central BCGs (see e.g. Hu, Cowie & Wang 1985; Heckman et al. 1989; Crawford & Fabian 1992; Donahue, Stocke & Gioia 1992) and also vast molecular gas and dust reservoirs (e.g. McNamara, O'Connell & Sarazin 1996; Donahue et al. 2000; Edge 2001; Jaffe, Bremer & van der Werf 2001; Edge et al. 2002; Salomé & Combes 2003).

Without some form of heating, the hot gas in these short central cooling time clusters would have had time to cool and condense, producing large quantities (10^{11}–10^{13} M$_\odot$) of cold gas and thousands of solar masses per year of star formation. Although signatures of cool and cold gas are observed in the central galaxies, in general, only ∼10 per cent of the predicted star formation is observed. The current paradigm is that some form of heating, most likely dominated by feedback from the central active galactic nucleus (AGN), is responsible for regulating the heating and cooling in these objects.

The optical emission-line nebulae surrounding the central galaxies in these systems have been found to extend to distances of ∼100 kpc in some objects and contain ∼10^4–10^7 M$_\odot$ of 10^4 K gas. The origin and excitation mechanisms of the extended optical emission-line systems have been much studied, but as of yet, no one mechanism has been found that can explain in detail all the features of emission.

Mechanisms proposed include photoionization by the central AGN (e.g. Heckman et al. 1989), photoionization by massive or extremely hot stars (e.g. Terlevich & Melnick 1985; Johnstone, Fabian & Nulsen 1987), heating through shocks (e.g. Cowie, Fabian & Nulsen 1980; Sabra, Shields & Filippenko 2000), conduction or mixing layers in the hot intracluster medium (ICM, e.g. Sparks, Macchetto & Golombek 1989; Crawford & Fabian 1992) and heating of the filaments through suprathermal particles (Ferland et al. 2008, 2009).

The heating and cooling in the Centaurus cluster is very well balanced despite the short central cooling time of only 200 Myr. NGC 4696 houses a radio source and multiple bubbles of relativistic gas. These are accompanied by soft X-ray filaments and a sharp rise

⋆E-mail: bcanning@ast.cam.ac.uk

Table 1. Observation log. [1]Observations are centred on NGC 4696. [2]Scan through galaxy.

Grism	Order sorting filter	Wavelength coverage (Å)	Exposure (s)	Field of view (arcsec^2)	Spectral resolution	Dispersion (Å pixel^{-1})
HRO[1]	GG435	5250–7400	35 100	27 × 27	2650	0.6
HRO[2]	GG435	5250–7400	5400	27 × 27	2650	0.6
HRB	Free	4150–6200	9000	27 × 27	2550	0.51
LRB	OS blue	4000–6700	2700	54 × 54	220	5.3

in the metal abundance in the central 30 kpc, among the highest seen in any cluster (approximately twice solar, Sanders & Fabian 2002; Fabian et al. 2005; Sanders & Fabian 2006). Centaurus also has one of the broadest range of measured X-ray temperatures, containing gas from 0.35 to 3.7 keV, over a factor of 10 in temperature (Sanders et al. 2008).

Crawford et al. (2005) presented narrow-band Hα+[N II] images showing the extensive, filamentary Hα nebulosity surrounding NGC 4696. This shares the morphology of the soft X-ray filaments and of a prominent dust lane. The origin of the complex and extensive filamentary system surrounding NGC 4696 has long been discussed with suggestions that the filaments have cooled from the ICM, are the result of a merger (Sparks et al. 1989) or have been drawn out into the ICM from the central galaxy by rising radio bubbles (Crawford et al. 2005). Recent work by Farage et al. (2010) found evidence in support of the merger origin and also presented evidence for shock excitation in the filaments. Our data suggest that the filaments are similar to those seen around many other BCGs, many of which have not recently undergone merger activity. We uncover a second velocity component in the central region which may be a filament extending behind the galaxy, and discuss the excitation mechanisms for the system.

The observations and data reduction are briefly described in Section 2, and their analysis, results and implications have been discussed in Section 3. In Section 4, we summarize our results and main conclusions. At the redshift of the Centaurus cluster (z = 0.0104, 44.3 Mpc), 1 arcsec corresponds to 0.210 kpc. Throughout this paper, we adopt $H_0 = 71$ km s^{-1} Mpc^{-1}, $\Omega_{\rm M} = 0.27$ and $\Omega_\Lambda = 0.73$.

2 OBSERVATIONS AND DATA REDUCTION

Observations were made on 2009 March 27–30 using the VIsible MultiObject Spectrograph (VIMOS) onboard the VLT in La Paranal, Chile [see LeFevre et al. 2003 and Zanichelli et al. 2005 for a description of the VIMOS Integral Field Unit (IFU) and a discussion of data-reduction techniques]. We obtained high-resolution orange (HRO), high-resolution blue (HRB) and low-resolution blue (LRB) data using the VIMOS IFU. We used the larger 0.67-arcsec fibres giving a field of view of 27 × 27 arcsec^2 with the HR grism and 54 × 54 arcsec^2 with the LR grism. Details of the observations are given in Table 1 and the HRO pointings are shown in Fig. 1.

The deep HRO data cover the wavelength of redshifted spectral lines of [N I] λ5199 to [O II] λ7330 including five coronal lines the details of which can be found in Canning et al. (2011). The HRB data cover the wavelength of redshifted lines of Hγ λ4341 to He I λ5875. An analysis of the stellar spectra in this object using the LRB data will be presented in Canning et al. (in preparation).

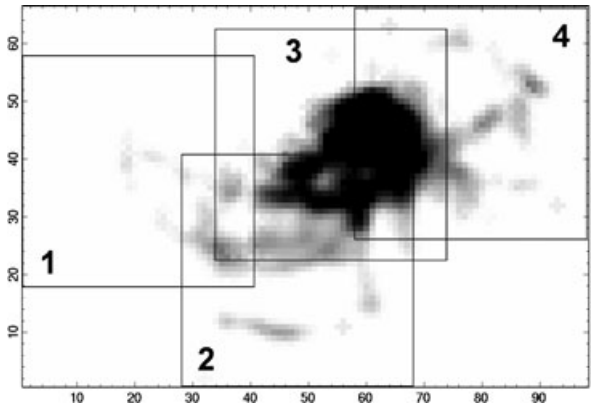

Figure 1. Our VIMOS [N II] λ6583 emission image of NGC 4696 overlaid with our VIMOS high-resolution pointings. The central RA and Dec. of box 1: $12^{\rm h}48^{\rm m}51\overset{\rm s}{.}4$, $-41^\circ18'42\overset{''}{.}8$; box 2: $12^{\rm h}48^{\rm m}49\overset{\rm s}{.}8$, $-41^\circ18'54\overset{''}{.}3$; box 3: $12^{\rm h}48^{\rm m}49\overset{\rm s}{.}5$, $-41^\circ18'39\overset{''}{.}8$; and box 4: $12^{\rm h}48^{\rm m}48\overset{\rm s}{.}0$, $-41^\circ18'37\overset{''}{.}3$ (all coordinates are in equinox J2000). The x- and y-axes are in pixels.

The data were reduced by the VIPGI[1] pipeline (Scodeggio et al. 2005). The resulting 3D data cubes were combined with a set of IDL routines (R. Sharp, private communication).

Instrument flexures in the VIMOS are dependent on the rotator position and suffer from hysteresis (Amico et al. 2008). For this reason, we took calibration frames (three flats and one arc) after each observation block. The observation blocks consisted of three science exposures. Each exposure was of only 15 min so as to minimize extreme flexures.

The wavelength calibration was done within VIPGI using He, Ne and Ar arc frames taken throughout the night. VIPGI performs a polynomial fit to the arc lines and we found that the rms deviations are approximately Gaussian with a mean of ∼0.05 Å and dispersion of ∼0.02 Å. This translates into an error in the velocity of ∼5 km s^{-1} which is significantly smaller than our full width at half-maximum (FWHM) instrumental resolution of 98 km s^{-1} (σ = 42 km s^{-1}).

Flux calibration was done using standard stars observed at the beginning and end of every night. Cosmic-ray rejection, final fibre-to-fibre transmission corrections, sky subtraction, extinction corrections and shifting to the object rest frame were performed outside VIPGI using IDL routines. Sky subtraction, where done, was complicated by the lack of suitable sky fibres and is described below.

Telluric absorption feature corrections for the O_2 and H_2O absorption in the 6000–7000 Å regime were determined from four observations of standard stars. The standard stars were observed at the beginning and the end of the night. Details of the correction are given in Appendix A.

[1] VIPGI (VIMOS Interactive Pipeline Graphical Interface) can be obtained from http://cosmos.iasf-milano.inaf.it/pandora/.

VIPGI's sky-subtraction technique is optimized for deep survey observations where the field is devoid of extended objects. Given this, we elect not to use VIPGI's sky-subtraction technique and instead use specific fibres shown to be lacking in emission lines associated with NGC 4696. We median-combine the spectra to find an average sky spectrum, remove the continuum by means of a spline fit, and scale and subtract the sky spectra from our object fibres. The line profiles are slightly different in each quadrant, so this process is performed on a quadrant-by-quadrant basis.

After basic reduction, transmission correction and corrections for sky absorption and emission, we bin the spectra in order to reach a chosen signal-to-noise ratio. We try two binning methods: the first bins on the basis of the surface brightness of emission in a 2D image by following contours of a smoothed image (Sanders 2006), while the second uses Voronoi tessellations to provide compact spatial bins (Cappellari & Copin 2003). The results of the two binning methods applied to a 2D image of [N II] λ6583 emission in NGC 4696 are shown in Fig. A2.

When binning spectroscopic data, one has to be careful not to bin over regions which are too extended. The spectral properties are unlikely to be similar in two distinct regions of a galaxy and thus binning these regions together would lead to spurious results. The Voronoi tessellation method of Cappellari & Copin (2003) provides more compact bins; however, the extended optical filament system of BCGs adds a further complication. These structures are extended in only one direction and as such the requirement for 'round' bins does not trace their morphology particularly well. Due to the filamentary structure of the optical-line nebulosity surrounding NGC 4696, we choose to bin our spectra using the contour-binning technique of Sanders (2006).

Our HRO and HRB spectra overlap between 5000 and 6000 Å. In order to incorporate all our data, we split the cubes into three wavelength regions. The regions chosen are 4000–5100, 5100–5800 and 5800–7500 Å. The two HR grisms used have a slightly different spectral resolution (see Table 1) with the resolution of the HRO grism being marginally larger than that of the HRB grism. In order to combine both data sets, it is necessary to re-bin the HRO spectra; details of the rebinning technique can be found in Appendix A.

The strong emission lines of Hα and the [N II] and [S II] doublets are fitted directly, on a pixel-to-pixel basis across the field of view. We fit these in the IDL using MPFIT (Moré 1978; Markwardt 2009). The weaker lines are first continuum-subtracted using template simple stellar population (SSP) models from Bruzual & Charlot (2003, hereinafter BC03), fitted using the STARLIGHT software package (Cid Fernandes et al. 2005, 2009). We use basefiles made up of 240 BC03 models spanning six metallicities, covering the range 0.005–2.5 $Z_{\odot}$, and 40 ages, covering the range 0–20 Gyr. An example of a fit to the stellar continuum between 4000 and 5200 Å is shown in Fig. 2. After continuum subtraction, the emission lines are fit using the same technique as for the stronger lines, described below. Where appropriate we impose the kinematics determined from the strongest emission features.

The five strongest emission features ([N II] λ6548, Hα λ6563, [N II] λ6583, [S II] λ6717 and [S II] λ6730) are fitted simultaneously. The redshift and velocity dispersion are constrained to be the same for one velocity component and the integrated flux of the [N II] doublet is tied, the scaling being dictated by the atomic parameters (Osterbrock & Ferland 2006). The spectrum is fitted between 6590 and 6820 Å. A continuum estimate is taken as the region between 6700 and 6750 Å, and subtracted from the spectrum. The continuum is fitted locally for the Hα+[N II] emission and the [S II] doublet.

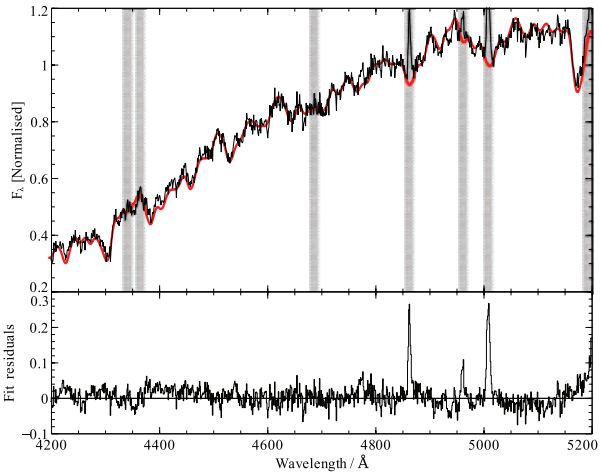

Figure 2. An example BC03 SSP model fit (red) to the observed spectrum (black) from bin 5 (60,46), between the wavelength of 4000 and 5200 Å. The fit residuals are shown in the bottom panel. Any regions where emission lines are expected are masked out in the fit. In the above plot, the masked regions correspond to the wavelengths of, from the left-hand to right-hand side, Hγ λ4341, [O III] λ4363, He II λ4686, Hβ λ4861, [O III] λ4958, [O III] λ5007 and [N I] λ5199.

An example of the fitting technique is shown in Fig. A5. We fit Gaussians to the spectra with one, two and three velocity components both with and without a broad Hα component. We perform an F-test to determine which fit to use, which is discussed further in Section 3.

3 RESULTS AND DISCUSSION

The line emission in the central regions of NGC 4696 is complex with many spectra requiring two velocity components to adequately fit the observed spectrum. We use the F-test statistic to determine which fit to use in the spectral modelling of a particular fibre. The F-test allows us to investigate the probability that the data follow the simpler of two proposed models nested within each other. We use MPFTEST in IDL to calculate the significance of the addition of extra parameters in the fit. We choose to accept the additional parameters when the probability falls below 0.01. The fits were examined by eye to ensure they were reasonable. Fig. 3 shows example fits to two bins; in the first, the F-test indicates a single Gaussian fit is sufficient to explain the data, while in the second, an additional velocity component is required. It was not found necessary to fit a broad Hα component. We adopt for the remainder of this paper the contour-binning method of Sanders (2006) and the appropriate F-test results (see Fig. A4).

The central region of NGC 4696 is exceedingly complex with many individual filaments, each of which is likely formed by narrower interwoven threads as in the case of the extended emission line system of NGC 1275 in the Perseus cluster (Fabian et al. 2008). The two velocity components detected in this central region are probably due to distinct filaments seen in projection and as such it is not obvious that splitting the emission into simple 'blueshifted' and 'redshifted' populations will lend any physical insight into this system.

In order to provide a more physical basis for the division of the two populations, we investigate the emission properties along the brightest inner filament. Fig. 4 shows, on the same scale, the

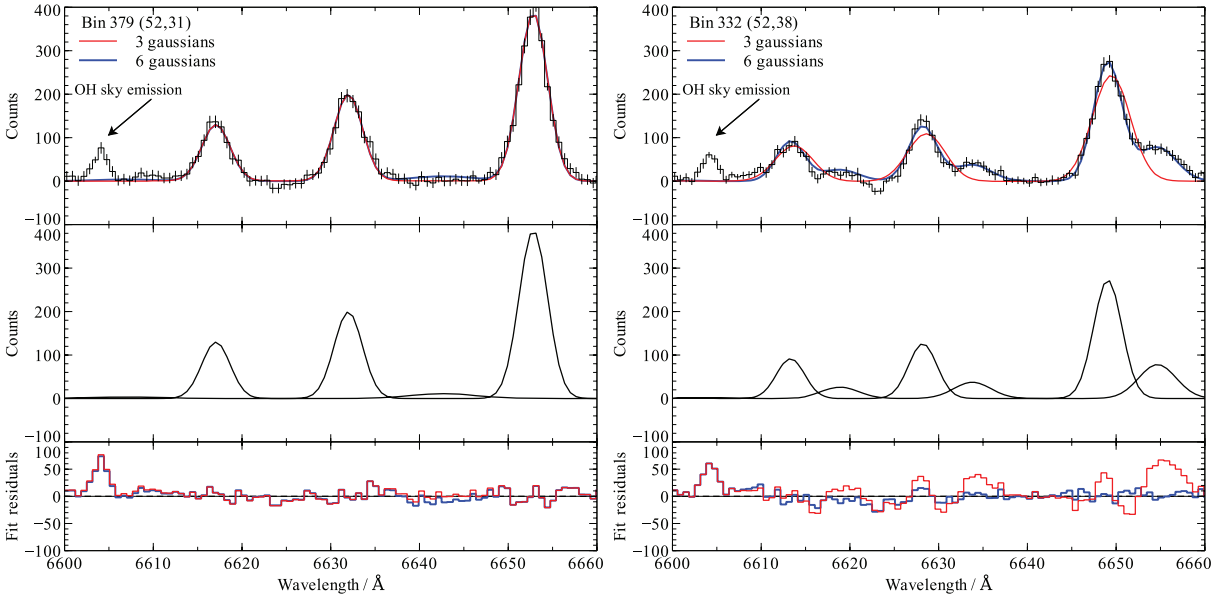

Figure 3. Example spectra with one and two velocity component fits from two pixels south-east of the centre of NGC 4696; the pixel coordinates in (x, y) and the corresponding 'bin' id are shown in the top left-hand corner of each plot. Both these spectra are within the spatial region where we have our deepest data. The top panel shows the data (black) and model (single Gaussian in red, double Gaussian in blue), the middle panel shows the separate Gaussian components of the two velocity component model and the lower panel shows the fit residuals: red residuals are data minus one velocity component model and blue residuals are data minus two velocity component models.

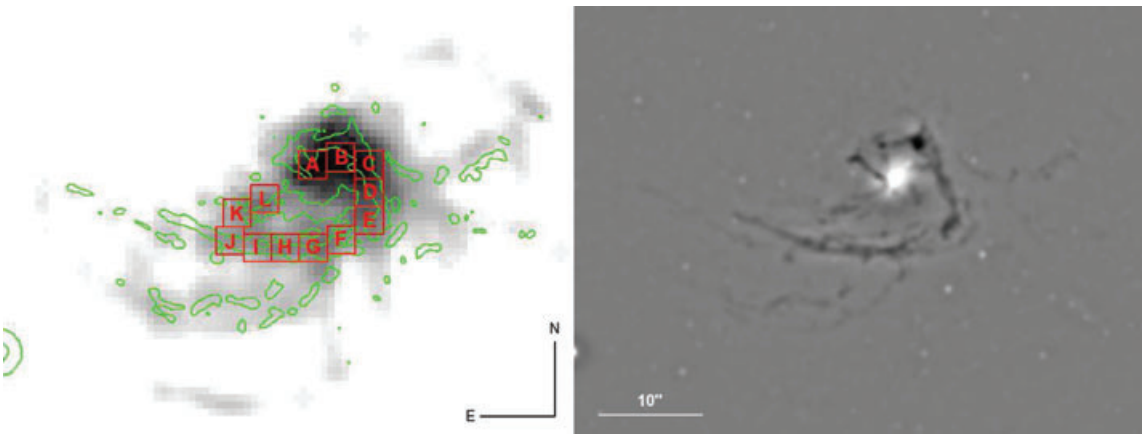

Figure 4. The left-hand image shows [N II] λ6583 emission. The bright ridge of emission which curls round the south-west of the nucleus is clearly visible. The ridge is binned in 2.5-arcsec^2 regions and labelled A–L with A starting near the nucleus. Overlaid are contours from an unsharp masked broad-band *HST* *F*435*W* image (shown on the right-hand side; both images have the same scale) tracing the dust lanes. The *HST* image has been smoothed by 20 and 5 pixels and the two resulting images subtracted.

[N II] λ6583 emission and dust lanes. There is a bright ridge of emission curling round the south-west of the nucleus which, in projection, coincides exactly with a large dust lane. We bin this region in 2.5 × 2.5 arcsec^2 bins (labelled from A to L in Fig. 4) and investigate the kinematic properties of the two velocity components were they to be separated based on redshift, velocity width and intensity; the results are presented in Fig. 5.

We would expect, if these two components followed emission from two distinct filaments, that the line-of-sight velocities and the FWHM velocity widths would vary smoothly with distance along the filament, by which we mean that the velocities are unlikely to jump dramatically from bin to bin along the filament length. From this argument and using the kinematical data, we rule out a division based on intensity (bottom panel of Fig. 5). To investigate further separating the components based on redshift and velocity width, we derive the intrinsic extinction from the Hα/Hβ ratio of each component. The results can be seen in Fig. 6 and imply that splitting the two velocity components based on the breadth of the emission is equivalent to distinguishing them based on intrinsic extinction, with the narrower component being more extinguished than the broader component in all regions where the Hα and Hβ lines could be detected at greater than 4σ. Splitting the components based on redshift provides no such distinction. From these results, we suggest that distinguishing the two components by velocity width as opposed to redshift is the more physical approach. The broad component lies closer to the nucleus, coincident with the dust lane, whereas the narrow component lies behind and is therefore more reddened. For the remainder of this paper, unless otherwise

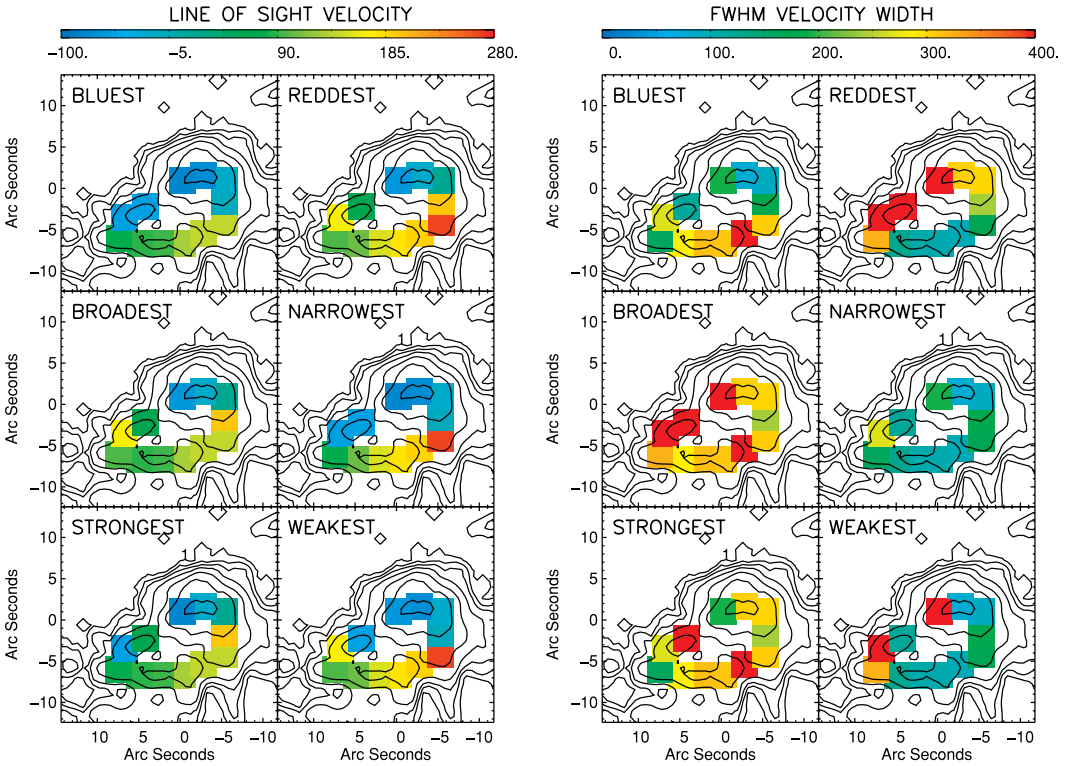

Figure 5. To establish a physical basis for distinguishing the two velocity components detected, we investigate the kinematic properties were the two components of the gas to be separated by redshift, velocity dispersion or intensity of emission along the bright inner filament. The figures show the most blueshifted (top left-hand panel), most redshifted (top right-hand panel), broadest (middle left-hand panel), narrowest (middle right-hand panel), strongest (bottom left-hand panel) and weakest (bottom right-hnd panel) components. Left-hand figure: the line-of-sight velocity in km s^{-1} of each component with respect to the velocity of NGC 4696 (3045 km s^{-1}). Right-hand figure: the FWHM velocity width in km s^{-1} of each velocity component. The (0,0) position corresponds to the nucleus at RA, Dec. = $12^{\rm h}48^{\rm m}49\overset{\rm s}{.}28$, $-41°18'39\overset{''}{.}4$.

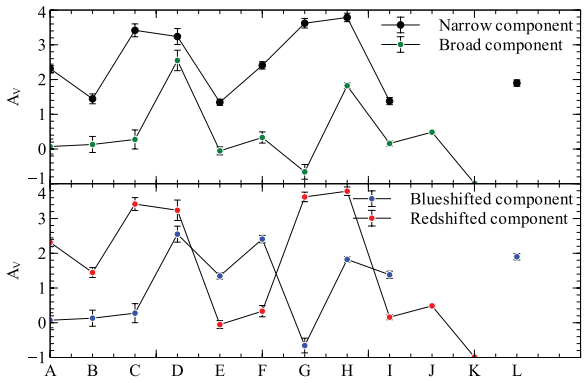

Figure 6. The intrinsic A_V extinction in the two velocity components derived from their Hα/Hβ ratio. The top panel shows the extinction were the components to be distinguished as a 'broader' and 'narrower' component and the bottom panel as a 'bluer' and 'redder' component. This figure shows splitting the two components based on the width of the line as opposed to the line centroid is equivalent to splitting the components based on the extinction of the emission.

stated, the two velocity components will be split into 'broader' and 'narrower' width components.

3.1 Reddening

We deredden the spectra for Galactic extinction using the reddening law of Calzetti et al. (2000) and an $E(B-V)$ value for the stellar continuum of 0.11 ($A_V = 0.34$). An extinction-to-reddening ratio, $R = A_V/E(B-V)$, of 3.1 is assumed for our Galaxy. This is done before shifting the spectra to their rest wavelength. A value for the intrinsic reddening is also estimated, where possible, from the Hα-to-Hβ line ratios (Fig. B1).

The logarithmic Hβ extinction coefficient, c, is calculated from the observed, $I_\lambda/I_{\rm H\beta}$, and intrinsic line ratios, $I_{\lambda 0}/I_{\rm H\beta 0}$,

$$\frac{I_\lambda}{I_{\rm H\beta}} = \frac{I_{\lambda 0}}{I_{\rm H\beta 0}} 10^{c[f(\lambda)-f({\rm H\beta})]}, \quad (1)$$

assuming a reddening law $f(\lambda)$. The extinction coefficient and reddening can therefore be calculated through

$$A_\lambda = -2.5cf(\lambda). \quad (2)$$

For the weaker Balmer line, we impose the kinematics of the strong emission lines and subtract the continuum using template SSP models as described in Section 2. The intrinsic extinction is calculated using the rest wavelengths of the lines and we assume a case B intrinsic recombination ratio. This method makes the assumptions that the dust is an obscuring screen, is homogeneous and that all the Hα and Hβ emission is from hydrogen recombination and none from collisional excitation.

The reddening map for a one-component velocity fit, on a per pixel basis, in the central regions of NGC 4696 is shown in Fig. B1. A single-component fit is presented as Hβ is weak and the second velocity component does not provide a good fit, unless the fibres are rather coarsely binned, as shown in Fig. 6. Contours of $E(B-V)$ derived from *HST* B- and I-band images and *Chandra* X-ray $N_{\rm H}$ column density (Crawford et al. 2005) are overlaid.

The regions where the value of intrinsic A_V is highest correspond well to the regions where $E(B-V)$ and $N_{\rm H}$ are greatest though the exact positions of the peaks are sometimes offset from those in the X-ray and broad-band optical maps. Crawford et al. (2005) find the regions of greatest extinction have a value of $A_V \sim 0.4$ which is in good agreement with previous studies (Jorgensen et al. 1983; Sparks et al. 1989). Our results, for the same knots, assuming a case B intrinsic Hα-to-Hβ line ratio (Osterbrock & Ferland 2006), are larger than this with the values of A_V in the range 1.5–2 for most of the knots along the dust lane. In order to make our results consistent with these previous imaging studies, we require an intrinsic Hα-to-Hβ line ratio of ∼4 (nearly 1.5 times the case B ratio) requiring a large component of collisional excitation to the hydrogen lines.

For Seyfert galaxies, radio galaxies and low-ionization nuclear emission-line regions (LINERs), the intrinsic Hα-to-Hβ line ratio is usually measured to be larger than the case B one, ∼3.1, due to the greater importance of collisional excitation in regions where there is a harder photoionizing spectrum (e.g. Veilleux & Osterbrock 1987). High ratios have also been seen in the case of the extended emission-line regions surrounding some BCGs. Kent & Sargent (1979) found a ratio of 4.77 in the filaments of NGC 1275, the BCG in the Perseus cluster. Gemini spectroscopy by Hatch et al. (2006) confirms high values of Hα/Hβ in the range 3–7 in the filaments. Voit & Donahue (1997) also find significant reddening in the filaments of Abell 2597 at 1.5 times the case B ratio. In both NGC 1275 and Abell 2597, the authors find no evidence of a deviation from the Galactic extinction laws. This implies the properties of the dust in the filaments are similar to that of our own Galaxy.

Sparks et al. (1989) found, from broad-band V and R images, that the dust extinction with wavelength behaves 'normally' in NGC 4696, that is, there is no evidence for a departure from the Galactic extinction laws. This makes formation of the filaments from the hot gas unlikely, and the authors favour a merger origin for the dust lane and filaments. More recently, it has been suggested that the dust lane could be the result of previous dusty star formation in the central galaxy which has been drawn out with the cool gas into filaments by radio bubbles rising in the ICM.

To make a comparison with the extinction corrections of Farage et al. (2010), we examine the extinction in a 3-arcsec-diameter region approximately 3 arcsec north-west of the nucleus (taken to be the centre of radio emission and of the X-ray point source, $12^{\rm h}48^{\rm m}49\overset{\rm s}{.}28$, $-41^\circ18'39\overset{''}{.}4$), where we find the peak in our Hα emission map. The coordinates of our chosen region are $12^{\rm h}48^{\rm m}49\overset{\rm s}{.}1$, $-41^\circ18'37\overset{''}{.}8$. Fitting the H$\alpha$ and Hβ emission with a single velocity component, as in Farage et al. (2010), we find the intrinsic A_V in this region is 0.33. Using the same values of the intrinsic emitted flux ratio (Hα/Hβ = 3.1) as Farage et al. (2010) gives a total A_V of 0.67. Using the case B ratio, the total A_V is 0.91. Our value differs from that of Farage et al. (2010) by 0.07; this is well within the error as a difference in the position of our region of 1.5 arcsec translates into a factor of almost 2 in Hα/Hβ.

As the reddening correction varies quite significantly across the field of view, due to the presence of the large dust lane, we elect to use the local value of Hα/Hβ where possible to correct our fluxes. Where this is not possible, we use the median value of $A_V = 0.9$.

3.2 Filament morphology

The detected line emission in our data follows closely the emission detected in the narrow-band Hα imaging of Crawford et al. (2005) (see Fig. 7). A central filament is seen with two velocity components extending 12 arcsec to the south-east of the nucleus. A further complex system of filaments extending over 25 arcsec to the north-west, south and east are also detected. Only the north-east appears devoid of filaments. All emission lines, with the exception of [O III], where the lines were strong enough not to impose the kinematics of the Hα emission, were found to have the same morphology as the Hα line, suggesting the emission occurs from the same gas. There also appear to be dust lanes present in all filaments except the weak southern-most filament (Fig. 4).

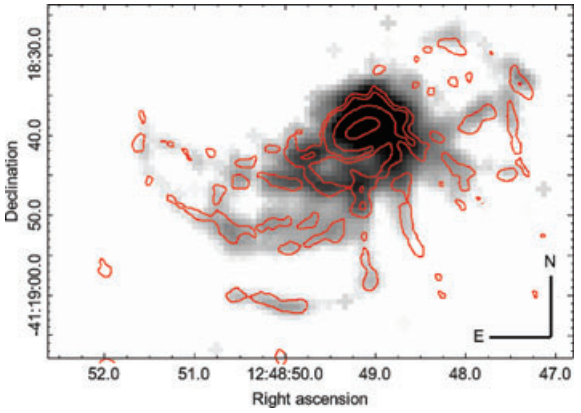

Figure 7. [N II] λ6583 emission (grey-scale) overlaid with contours of Hα from the narrow-band imaging of Crawford et al. (2005). The morphologies of other emission lines follow generally that of the [N II] λ6583 emission.

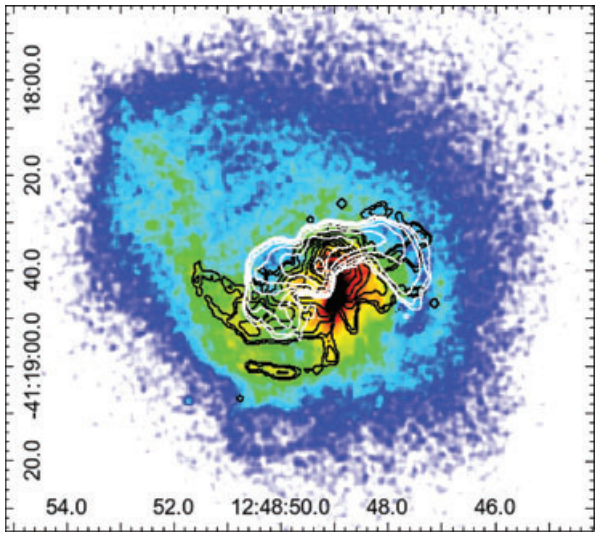

Figure 8. Soft X-ray emission (0.5–1.5 keV) of the centre of NGC 4696. Contours of [N II] λ6583 emission are overlaid in black and 5-GHz radio contours in white.

The emission-line gas traces well the inner regions of the soft X-ray filaments (Fig. 8). However, the soft X-ray filaments extend much farther up to the north-east of the galaxy, leading towards a depression in the X-ray gas thought to be a ghost bubble, of plasma from the radio source, rising buoyantly from the nucleus (Crawford et al. 2005). The area just north-east of the nucleus, devoid of both optical emission-line gas and soft X-ray filaments, coincides with a prominent radio bubble.

The two velocity components have a different morphological structure. Fig. 9 shows the [N II] λ6583 line emission in this central region, smoothed by a Gaussian with FWHM 3.1 arcsec (σ = 1.3 arcsec, 2 pixels). The left-hand image is the emission from the broader component and shows two clear peaks in emission. The

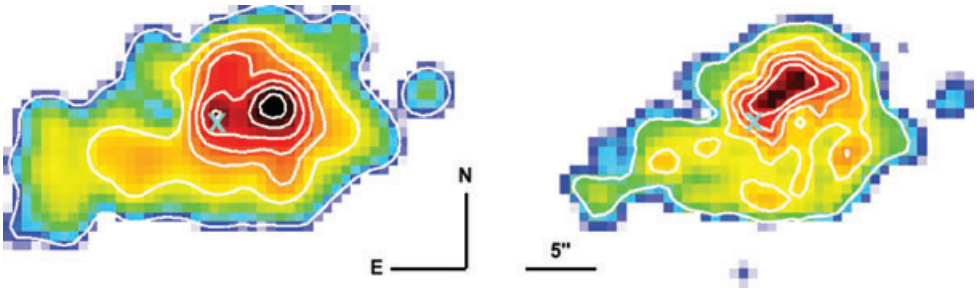

Figure 9. The morphologies of the broader (left-hand figure) and narrower (right-hand figure) velocity components. The peak in the emission between the two components is offset by ∼2 arcsec. The broader component has a much more circular profile, while the narrow component has a steeper central peak and exhibits a less smooth structure. The two images have been smoothed by a Gaussian with FWHM 3.1 arcsec ($\sigma = 1.3$ arcsec) and are plotted on the same spatial scale; the cyan 'X' marks the nucleus. The intensity scale has been adjusted individually to achieve the best contrast.

weaker peak to the east coincides with the centre of radio emission and the weak X-ray point source ($12^h48^m49^s.28$, $-41°18'39''.4$, Taylor, Fabian & Allen 2002); throughout this paper, we define the nucleus as this point. 5 arcsec to the west is the point of largest flux for the broad emission component. The surface brightness contours show the emission about this point is smooth and circular in the central 5 arcsec before stretching towards the south-east of the nucleus. The right-hand image shows the narrow emission component which is far less smooth in morphology. The emission peaks in a bar stretching north-west from the nucleus and then curls clockwise round the nucleus. We find the contours of surface brightness of both these components deviate from that of the dust near the nucleus, as found by Farage et al. (2010).

Fig. 10 shows a single component fit to the [O III] λ5007 emission (left-hand image), beside an [N II] λ6583 single-component-fit emission map (right-hand image). The [O III] emission is weakly detected in the inner filament (we do not have a HRB pointing in the outer regions) but very strong near the centre of radio emission. The second peak of [O III] emission to the west which coincides with the peak in the other emission lines is much weaker, implying much of the [O III] emission in the central regions is associated with the AGN.

Sparks et al. (1989) and Farage et al. (2010) suggest NGC 4696 has an intrinsically one-sided spiral structure due to the apparent close association of the main dust lane with line emission. While we also observe a strikingly very close correspondence between the optical filaments and the many dust lanes of NGC 4696 (see Fig. 4), our detection of at least two velocity components to the optical emission-line gas, exhibiting different extinction properties, provides evidence contrary to this suggestion. NGC 4696 is clearly a very complex galaxy surrounded by an intricate filamentary system. The high extinction of the narrow velocity component and its less smooth morphology is interpreted as a filament located behind the main, more centrally located broader emission-line component.

3.3 Emission-line fluxes

The spectrum of a region with a radius of 10 arcsec centred on the radio core, with and without continuum subtraction, is shown in Fig. 11, with the strongest lines marked. The spectrum is similar to other filament emission in cool-core BCGs, showing strong low-ionization emission lines. NGC 4696 has stronger [O III] λ5007 emission than found in NGC 1275 or Abell 2597 though the majority of this emission coincides with the nucleus and is likely associated with the AGN.

We compare the dereddened flux in Hα emission to that of Crawford et al. (2005). Using narrow-band Hα imaging, the authors find a surface brightness in the inner (∼8 arcsec from the radio core) filaments of 3.5×10^{-16} erg cm^{-2} s^{-1} arcsec^{-2} and in the fainter outer filaments (∼27 arcsec) of 1.4×10^{-16} erg cm^{-2} s^{-1} arcsec^{-2}. They obtain a lower limit on the total Hα luminosity beyond a radius of 3.5 arcsec of 1.5×10^{40} erg s^{-1}. Our data are consistent with these with the average surface brightness of the filaments 8 and 27 arcsec from the radio core being 2.2×10^{-16} and 1.3×10^{-16} erg cm^{-2} s^{-1} arcsec^{-2}, respectively. We obtain a total extinction-corrected Hα luminosity beyond a radius of 3.5 arcsec of 1.7×10^{40} erg s^{-1} and a total extinction-corrected Hα luminosity of 2.2×10^{40} erg s^{-1}. Our derived Hα and [N II] fluxes and luminosities are slightly larger than, though still consistent with, those of Farage et al. (2010). This is expected as our HRO data probe more of the filament system.

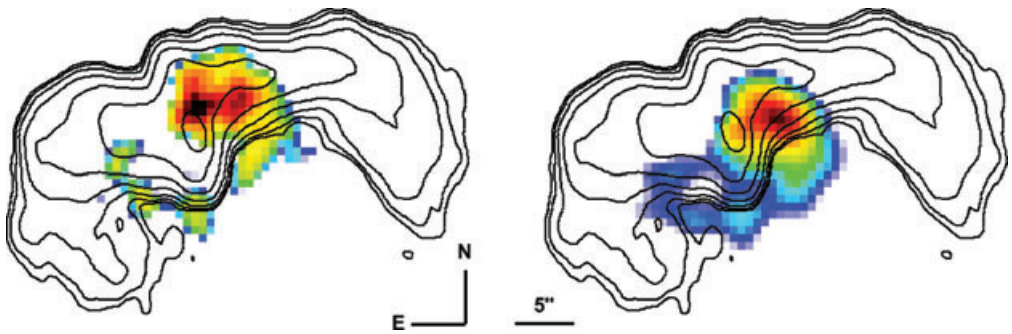

Figure 10. The [O III] λ5007 (left-hand figure) and [N II] λ6583 (right-hand figure) emission in the central region of the galaxy. The peak in emission is offset by ∼4 arcsec between the two images. The two images have been smoothed by a Gaussian with FWHM 3.1 arcsec ($\sigma = 1.3$ arcsec) and are plotted on the same spatial scale. The intensity scale has been adjusted individually to achieve the best contrast.

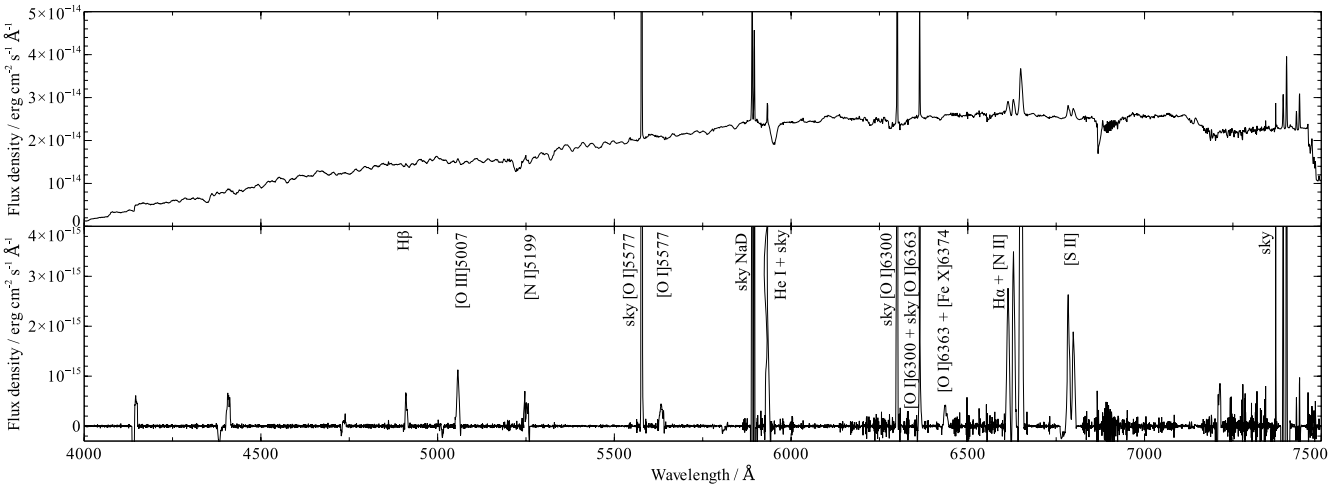

Figure 11. Top panel: the spectrum of NGC 4696 within a radius of 10 arcsec; sky lines that are confused with object emission are not subtracted. Bottom panel: the same spectrum after continuum subtraction using BC03 models. Object emission lines and confused sky lines are labelled.

Table 2. Total fluxes and luminosities of emission lines in NGC 4696 after correction for extinction using the median $A_V = 0.9$. Emission lines bluewards of 5100 Å are measured only in the inner 27 arcsec as we do not have HRB data beyond this. Where the lines are marked by < the value indicates a 90 per cent upper limit ($\Delta\chi^2 = 2.7$). Where the lines are marked with ** the object emission was confused with other emission or sky lines and it was necessary to fit these simultaneously. All values are determined after subtraction of the continuum.

Line	Total flux (erg cm^{-2} s^{-1})	Total luminosity (erg s^{-1})	Flux/$F_{\mathrm{H}\alpha}$
Hγ λ4341	$<2.2 \times 10^{-15}$	$<4.9 \times 10^{38}$	0.02
[O III] λ4363	$<1.5 \times 10^{-15}$	$<3.3 \times 10^{38}$	0.01
He II λ4686	$<2.4 \times 10^{-15}$	$<5.5 \times 10^{38}$	0.02
Hβ λ4861	$2.0 \times 10^{-14} \pm 9.9 \times 10^{-16}$	$4.5 \times 10^{39} \pm 2.3 \times 10^{38}$	0.20
[O III] λ4958	$9.2 \times 10^{-15} \pm 1.2 \times 10^{-15}$	$2.1 \times 10^{39} \pm 2.8 \times 10^{38}$	0.09
[O III] λ5007	$2.8 \times 10^{-14} \pm 5.5 \times 10^{-16}$	$6.3 \times 10^{39} \pm 1.3 \times 10^{38}$	0.28
[N I] λ5199	$5.4 \times 10^{-15} \pm 1.3 \times 10^{-15}$	$1.2 \times 10^{39} \pm 2.9 \times 10^{38}$	0.06
[C V] λ5309	$<6.0 \times 10^{-16}$	$<1.4 \times 10^{38}$	0.01
[O I] λ5577	$<2.9 \times 10^{-15}$	$<6.6 \times 10^{38}$	0.03
[N II] λ5755	$<4.2 \times 10^{-15}$	$<9.6 \times 10^{38}$	0.04
He I λ5875**	$1.6 \times 10^{-14} \pm 1.4 \times 10^{-15}$	$3.8 \times 10^{39} \pm 3.3 \times 10^{38}$	0.17
[O I] λ6300**	$1.7 \times 10^{-14} \pm 4.0 \times 10^{-15}$	$4.0 \times 10^{39} \pm 9.0 \times 10^{38}$	0.18
[O I] λ6363**	$5.7 \times 10^{-15} \pm 3.0 \times 10^{-15}$	$1.3 \times 10^{39} \pm 7.0 \times 10^{38}$	0.06
[N II] λ6548	$5.4 \times 10^{-14} \pm 1.3 \times 10^{-14}$	$1.2 \times 10^{40} \pm 3.0 \times 10^{39}$	0.56
Hα λ6563**	$9.8 \times 10^{-14} \pm 5.9 \times 10^{-15}$	$2.2 \times 10^{40} \pm 1.4 \times 10^{39}$	1.00
[N II] λ6583	$1.8 \times 10^{-13} \pm 9.5 \times 10^{-15}$	$4.2 \times 10^{40} \pm 2.2 \times 10^{39}$	1.87
[S II] λ6717	$5.5 \times 10^{-14} \pm 5.7 \times 10^{-15}$	$1.3 \times 10^{40} \pm 1.3 \times 10^{39}$	0.56
[S II] λ6731	$4.5 \times 10^{-14} \pm 5.2 \times 10^{-15}$	$1.0 \times 10^{40} \pm 1.2 \times 10^{39}$	0.46
[Ca II] λ7291**	$<1.7 \times 10^{-14}$	$<3.9 \times 10^{39}$	0.18
[O II] λ7320**	$<3.7 \times 10^{-14}$	$<8.4 \times 10^{39}$	0.38
[Ca II] λ7325**	$<3.7 \times 10^{-14}$	$<8.5 \times 10^{39}$	0.38
[O II] λ7330**	$<2.1 \times 10^{-14}$	$<4.8 \times 10^{39}$	0.21

The total luminosities of all detected lines and the 90 per cent upper limits of emission lines not found in our spectra are given in Table 2. Emission lines are fitted as described in Section 2, although some lines are confused with other emission lines or sky emission and therefore warrant special attention. He I, [O I] λ6300, Hα, [Ca II] and emission lines of [O II] suffer from confusion with sky emission; in each of these cases, the sky emission is fitted simultaneously with the object emission lines. The red wing of the [O I] λ6363 emission line coincides with the [Fe X] λ6374 emission line discussed in Canning et al. (2011). The flux of this line is linked by atomic physics to the flux of the [O I]λ6300 emission and we fit these, the sky [O I] lines and the [Fe X] λ6374 emission line together. We only have HRB data from the central ∼27 arcsec of NGC 4696; therefore, all emission lines bluewards of 5100 Å may be lower limits.

3.3.1 [O III] emission

A characteristic of the extended optical emission filaments in many BCGs is their low [O III] emission with respect to the hydrogen recombination lines (see e.g. Hatch et al. 2006) and surprisingly high [Ne III] emission lines (see discussion of charge exchange in

Ferland et al. 2009). The ionization potential of Ne^+ is greater than that of O^+, so if we observe [Ne III] lines, we would expect to see those of [O III] as well.

The total [O III] λ5007 emission in NGC 4696 is fairly strong with an [O III] λ5007/Hβ λ4861 intensity ratio measured as 1.4 in the inner 27×27 arcsec^2 (the field-of-view of our HRB grism). However, as discussed in Section 3.2, the surface brightness of [O III] emission is steeply peaked and located near to the centre of radio emission. It is therefore probable that much of the [O III] emission is due to the central AGN.

We investigate this possibility by choosing two regions: one coincident with the radio nucleus (region A) and the other offset by ∼12 arcsec, on the farthest edge of the inner filament from the nucleus (region B). Spectra are extracted in both regions from a 3 pixel (2 arcsec) radius circle; the regions are shown in Fig. 12 and the spectral regions containing the Hβ line and [O III] emission are shown in Fig. 13. The ratio of [O III] λ5007 to Hβ λ4861 clearly varies in the two regions with the central region having a ratio of ∼2 and the filament emission having a

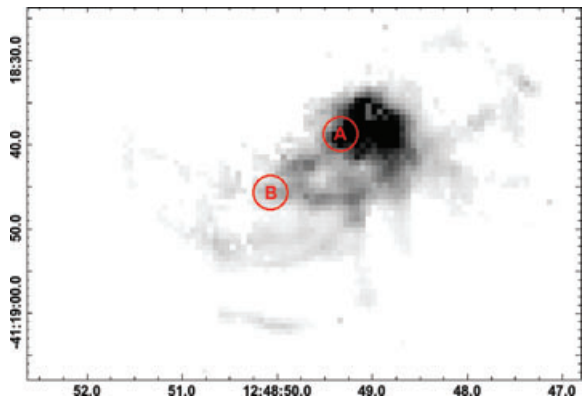

Figure 12. Regions A and B, both 3 pixels in radius. Region A is coincident with the nucleus defined as the centre of radio emission ($12^h48^m49^s.28$, $-41°18'39''.4$; Taylor et al. 2002), while region B is ∼12 arcsec to the south-east of the nucleus, on the outer edge of the inner filament.

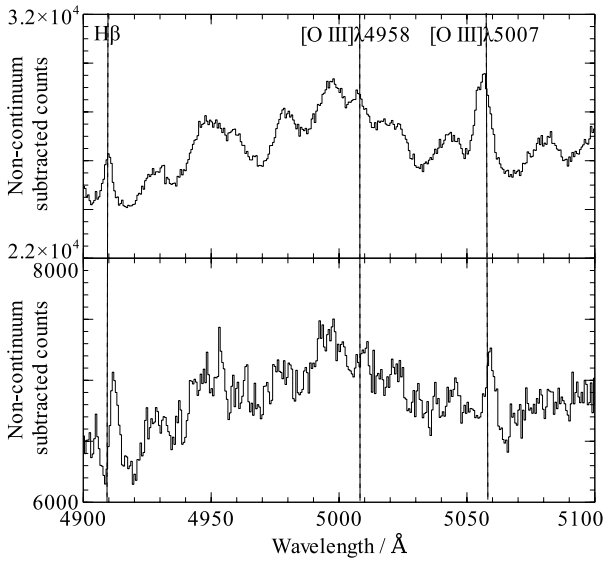

Figure 13. The non-continuum-subtracted HRB spectra in regions A (top panel) and B (bottom panel). The [O III] λ5007/Hβ λ4861 ratio varies dramatically from ∼2 (region A) to ∼0.7 (region B, see Table 3).

Table 3. Extinction-corrected $F_\lambda/F_{H\alpha}$ in regions A and B (see Fig. 12). Region A coincides with the nucleus, defined as the centre of radio emission, while region B is a point ∼12 arcsec away on the north-eastern edge of the inner filament. Where the lines are marked with **, the object emission was confused with other emission or sky lines and it was necessary to fit these simultaneously. The measured Hα fluxes in the two regions are: $F_{H\alpha A} = 5.29 \times 10^{-15}$ erg cm^{-2} s^{-1} and $F_{H\alpha B} = 2.99 \times 10^{-15}$ erg cm^{-2} s^{-1}.

Line	$F_\lambda/F_{H\alpha A}$	$F_\lambda/F_{H\alpha B}$
Hβ λ4861	0.37	0.23
[O III] λ4958	0.26	–
[O III] λ5007	0.77	0.15
[N I] λ5199	0.23	0.19
He I λ5875**	0.15	–
[O I] λ6300**	0.18	0.21
[O I] λ6363**	0.06	0.07
[N II] λ6548	1.04	0.57
Hα λ6563**	1.00	1.00
[N II] λ6583	3.10	1.70
[S II] λ6717	0.92	0.39
[S II] λ6731	0.58	0.33

much lower [O III] λ5007/Hβ λ4861 of only ∼0.7. Ratios of the fluxes of the detected lines to Hα for the two regions are shown in Table 3.

Observations of the inner regions of NGC 1275 (Kent & Sargent 1979; Sabra et al. 2000) have found [O III] λ5007/Hβ λ4861 of 0.6 in the inner 24 arcsec (8 kpc); however, the [O III] λ5007 emission in the outer filaments, beyond 10 kpc, is not detected in the long-slit spectra of Hatch et al. (2006). The authors are able to put an upper limit on the [O III] λ5007/Hα λ6563 emission in a region 18 kpc from the nucleus of <0.03; their limit on [O III] λ5007/Hβ λ4861 is <0.13.

Using long-slit spectra from the INT and FOS spectra, Johnstone & Fabian (1988) found that [O III] λ5007/Hβ λ4861 decreases away from the core in both NGC 1275 and Abell 1795. In NGC 1275, their spectra extend to a radius of 8 kpc where they find the ratio drops by a third from the central value to about 0.5. Similarly, in Abell 1795, the ratio peaks at about 1 in the nucleus and decreases to ∼0.6 at the outer extent of the slit which corresponds to a radius of 6 kpc. Low values of [O III] λ5007/Hβ λ4861 have also been observed in the vast emission-line nebula associated with the BCG of Abell 2597 (Voit & Donahue 1997).

Shock models tend to predict higher [O III] λ5007/Hβ λ4861 intensity values and larger fluxes of [O III] λ4363 than those seen in the outer extents of the emission-line nebulae surrounding these objects (Voit & Donahue 1997; Sabra et al. 2000). We obtain only upper limits on the [O III] λ4363 emission across the field of view with the upper limit on the [O III] λ4363/Hβ λ4861 intensity values of ∼0.08. Unfortunately, we only acquired one pointing of HRB data in NGC 4696 and so are unable to investigate the ratio in the very outer extent of the nebulae.

Our spectra do not extend far enough into the blue to observe the [Ne III] λ3869 optical line; however, Farage et al. (2010) have detected this at the 3σ level (see their fig. 3). The

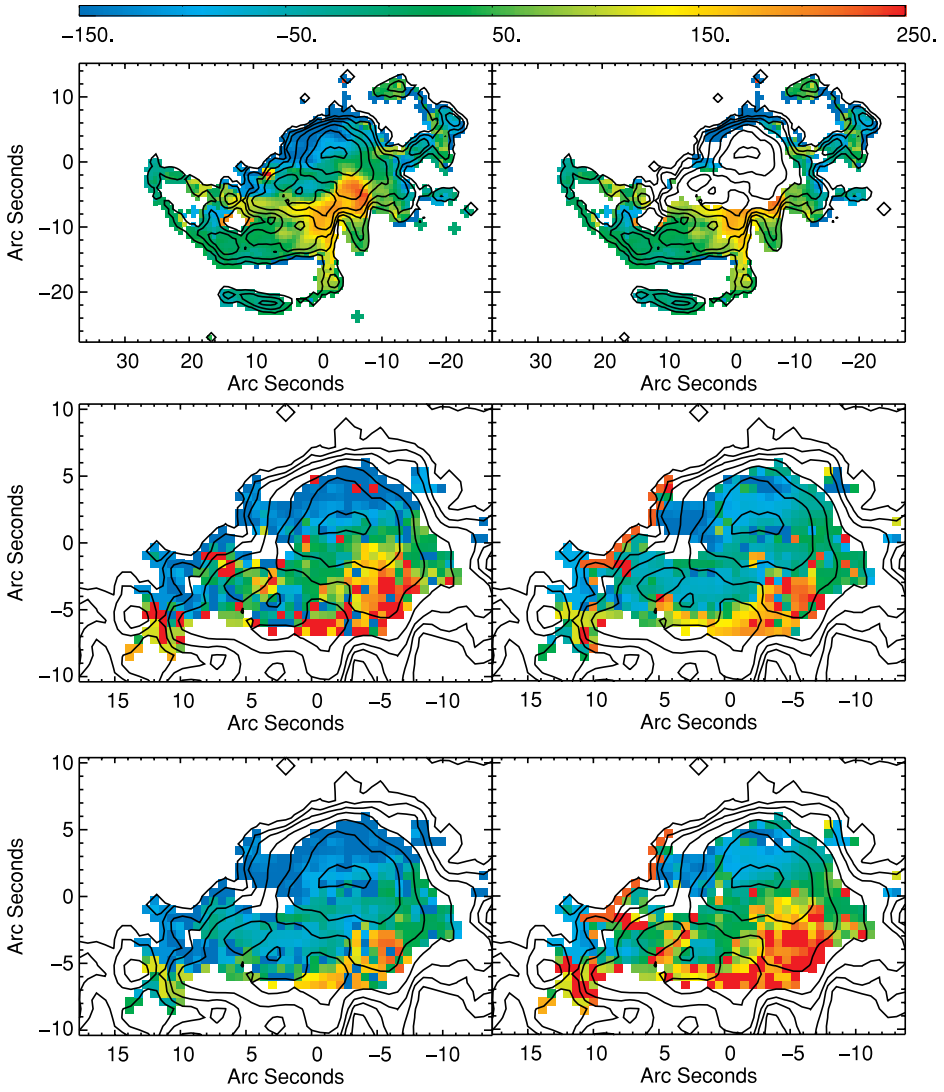

Figure 14. Top row: (left-hand panel) the line-of-sight velocity relative to the velocity of the galaxy, 3045 km s^{-1} ($z = 0.010\,157$), from Postman & Lauer (1995), if a single-component fit is made over the whole field of view, and (right-hand panel) the line-of-sight velocity shown only where one velocity component was found to be sufficient. The figures shown are fits from the strong [N II] λ6583 emission line. Middle row: the same as the above for the two-component fit. The left-hand plot indicates the broader component and the right-hand plot the narrower component. Bottom row: the blueshifted (left-hand panel) and redshifted (right-hand panel) velocity components. The colour bar is in units of km s^{-1} and the axis (0,0) position corresponds to RA, Dec. = $12^{\rm h}48^{\rm m}49\overset{\rm s}{.}28$, $-41^\circ18'39\overset{''}{.}4$, coinciding with the core of the radio emission.

infrared line of [Ne III] λ15.56 μm has also been clearly detected using *Spitzer* Infrared Spectrograph (IRS) short-high (SH) spectra by Johnstone et al. (2007). Photoionization models for the excitation of the emission-line nebulae struggle to account for the anomalously low [O III] yet high [Ne III] emission unless coupled with high metallicities. Sanders & Fabian (2006) find the O and Ne abundances to peak at about solar towards the centre of the Centaurus cluster. However, the measured Ne abundance is highly dependent on the spectral model and varies between 0.5 and 2 between the SPEX and APEC models.

Particle ionization models put forward by Ferland et al. (2008, 2009) have so far been successful at reproducing the observed ratios due to the importance of charge transfer. Using CLOUDY simulations (last described by Ferland et al. 1998), the authors find the charge-transfer recombination of O^+ and O^{+2} is very fast compared to that of He^+, Ne^+ and Ne^{+2}, resulting in significant [Ne II] and [Ne III] emission compared with [O III].

3.4 Velocity structure

Maps of the kinematics of the optical emission-line nebulae are shown in Figs 14 and 15. The line-of-sight velocities are given with respect to the redshift of NGC 4696 determined to be $z = 0.010\,157$ (3045 km s^{-1}) by Postman & Lauer (1995). The velocity dispersions are presented as the FWHM velocities measured from the Gaussian fits to the strongest emission lines in our spectra and have been corrected for the measured instrumental width, determined from fitting sky lines close to the observed Hα emission line (FWHM 98 km s^{-1}, $\sigma = 42$ km s^{-1}). All emission lines strong enough to map were found to have essentially the same velocities, as seen in Farage et al. (2010); therefore, we show maps of only [N II] λ6583.

3.5 Central velocity structure

The line-of-sight velocity of the central region of the galaxy changes smoothly by ∼400 km s^{-1} across the north to south direction with

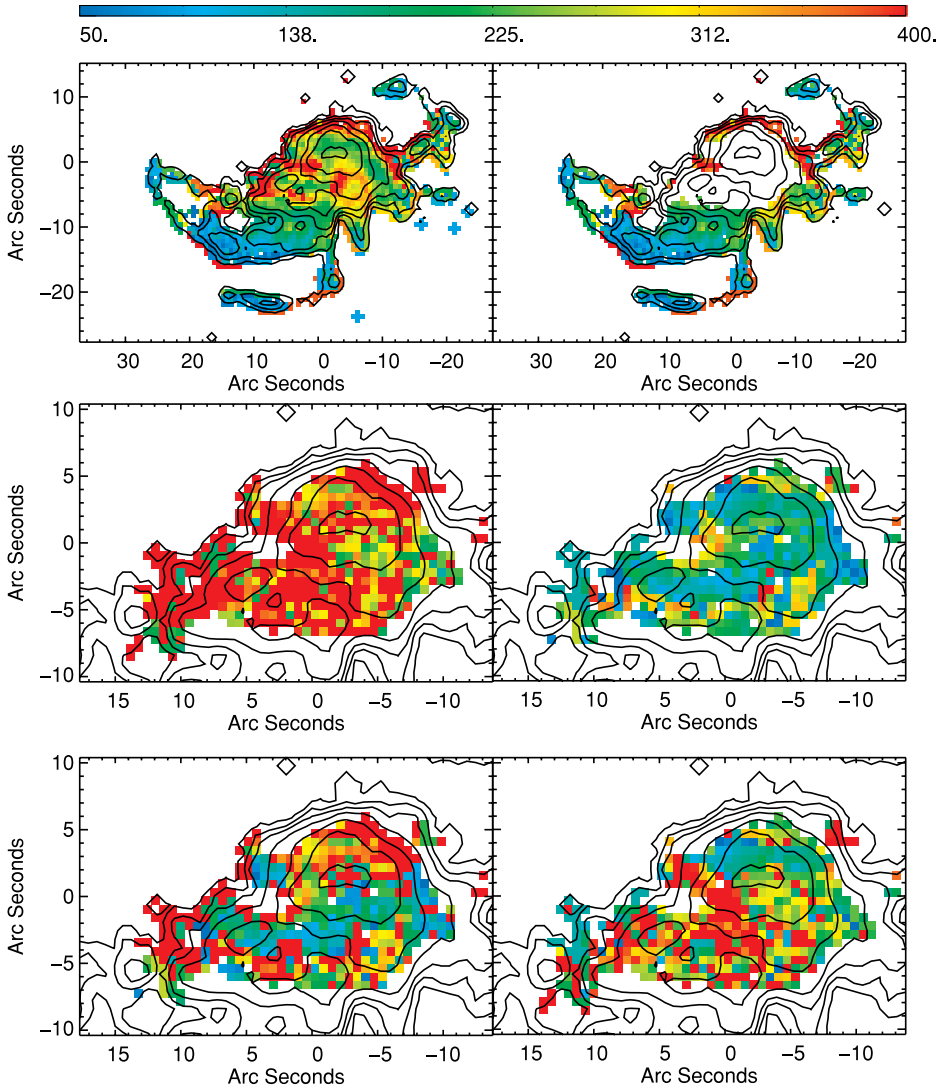

Figure 15. Top row: (left-hand panel) the velocity width at FWHM if a single-velocity-component fit is assumed over the whole field of view and (right-hand panel) the velocity width where only one velocity component is found to be sufficient. The figures shown are fits from the strong [N II] λ6583 emission line. Middle row: the same as the above for the two-component fit. The left-hand plot indicates the broader component and the right-hand plot the narrower component. Bottom row: the blueshifted (left-hand panel) and redshifted (right-hand panel) velocity components. The colour bar is in units of km s^{-1} and has been corrected for the instrumental width. The axis (0,0) position corresponds to RA, Dec. = $12^{h}48^{m}49^{s}.28$, $-41^{\circ}18'39''.4$, coinciding with the core of the radio emission.

the southern region being more redshifted, perhaps indicating a component of rotation of the nebula about the nucleus. This gradient in velocity structure is seen in both the broad and narrow velocity components but to different extents (see Fig. 16).

The broad component has a wider distribution of line-of-sight velocities, with the northern-most and southern-most velocities varying by ∼500 km s^{-1}, while in the narrow component, the velocity changes by ∼250 km s^{-1} from the northern-most to southern-most regions. This limited range in velocities is similar to those observed in the extended filaments seen to the north-west, south and east of the nucleus.

The broad velocity component has a FWHM of ∼300–400 km s^{-1}, while the narrow component has width in the range 50–200 km s^{-1}. The linewidths of both components are much greater than the thermal widths of the hydrogen gas which is broadened by ∼10 km s^{-1} at 10^4 K, implying the gas is broadened either by shocks or by turbulence.

3.6 Outer filaments

The distribution of line-of-sight velocities of the outer filaments is less than the central region, with a range of ∼200 km s^{-1} in most cases. We bin the outer emission in 3 × 3 arcsec^2 bins to examine the velocity structure more closely along the length of the filaments, which results are shown in Fig. 17. The line-of-sight velocity zero-point is taken as 3045 km s^{-1}.

The eastern filament is the dominant structure curling round the south-east of the galaxy, coinciding closely with the outer dust lanes and soft X-ray filaments. The Hα imaging of Crawford et al. (2005) shows this filament is in fact made of several thinner threads such as those resolved in NGC 1275 (Fabian et al. 2008). The filament extends over 30 arcsec (6 kpc) from the nucleus but exhibits a very narrow distribution in line-of-sight velocities peaking at the same velocity as the galaxy (see Fig. 16). The low velocities suggest we are viewing this filament close to the plane of the sky. Both the

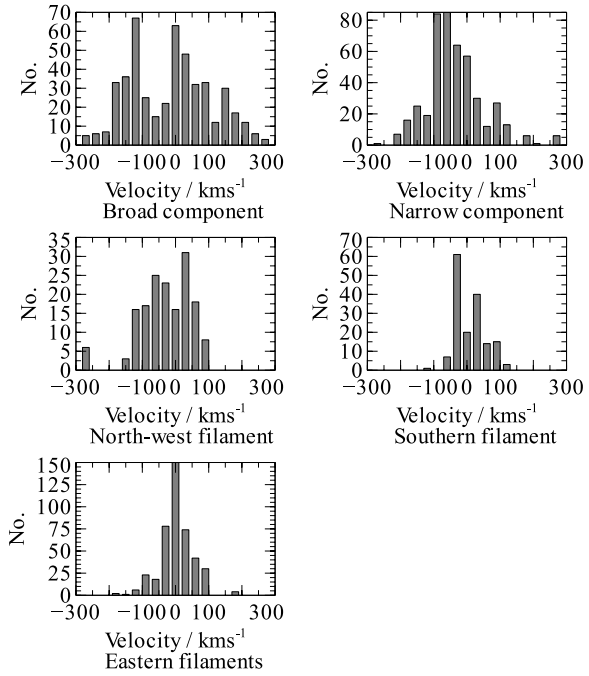

Figure 16. The distribution of line-of-sight velocities in the filaments and central regions.

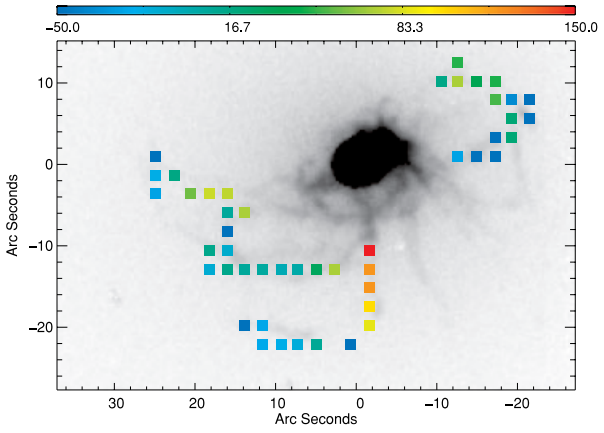

Figure 17. The line-of-sight velocities in the outer filaments. The velocity zero-point is taken as 3045 km s^{-1}.

eastern filament and the north-west filament appear to curve round the radio bubble. The north-west filament has a larger variation in line-of-sight velocities, though the variation is still smooth, with the innermost part more blueshifted and the outermost part more redshifted.

The southern filament exhibits a divide in line-of-sight velocity along the filament length such as found by Hatch et al. (2006) in the northern filament of NGC 1275. The northern-most part, closest to the nucleus, displays a redshift of ∼140 km s^{-1}, whereas the region farthest from the nucleus displays a blueshift of ∼−50 km s^{-1}. The regions closest and farthest from the nucleus along this filament may thus be moving in opposite directions with the filament either collapsing in or stretching out; however, the filament is clearly curved and this scenario is complicated by projection effects.

The velocity widths of the emission lines in the outer filaments are fairly low, ranging from 50 to 250 km s^{-1} with the more northern filaments having a slightly larger velocity width than the southern ones. The range of velocity widths measured in these filaments is similar to those seen in the Perseus cluster (Hatch et al. 2006).

3.7 Implications for filament origin

Kinematically, the central narrow emission-line component bears more similarity to the outer filaments than the broad component having both a lower velocity dispersion and a narrower distribution of line-of-sight velocities. This supports the interpretation of the narrow component being a separate filament farther from the nucleus, seen in projection with the main central broad component. This would suggest the filamentary system is not an intrinsically one-sided spiral structure and it is unclear how a merger origin could account for the diversity in morphology and kinematics of these filaments.

If the filaments had an inflow origin, as predicted by early cooling flow models (Fabian, Nulsen & Canizares 1984), we would expect that there would be a negative radial gradient in the widths of the emission lines due to both greater acceleration towards the centre and line-of-sight effects (Heckman et al. 1989). This is not observed in any of the outer filaments with the velocity dispersion being largely unvarying with the exception of the north-west filament where the velocity dispersion appears erratic along the filament. This filament exhibits knots in the Hα image, just north-east of the bend in the filament and again at the end. Another fainter filament is also present in the Hα image, which crosses or joins the north-west filament at this bend where the measured velocity width is largest (see Fig. 18). It is therefore likely that the measured velocity width in this region is large and erratic due to two or more filaments overlapping, in the line of sight, with slightly different velocities and resulting in a broad, strong peak of emission.

Crawford et al. (2005) suggest the filamentary system is the consequence of buoyantly rising radio bubbles which draw filaments of cool and cold gas and dust up from beneath them as has also been seen in other brightest cluster galaxies (Bohringer et al. 1995; Churazov et al. 2001; Fabian et al. 2003; Reynolds et al. 2005; Hatch et al. 2006). This is supported by a depression in the X-ray intensity and thermal pressure maps to the north-east of the nucleus, just beyond the optical and soft X-ray filaments (see their fig. 5). A similar depression is seen in the south-west, and low-frequency (330-MHz) radio emission also extends towards both these structures. The kinematics of the filaments are consistent with this picture with smoothly varying line-of-sight velocities and low

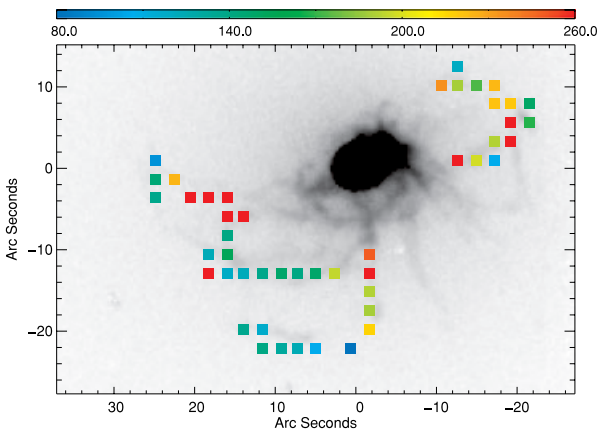

Figure 18. The FWHM velocity widths in the outer filaments after correction for the instrumental width.

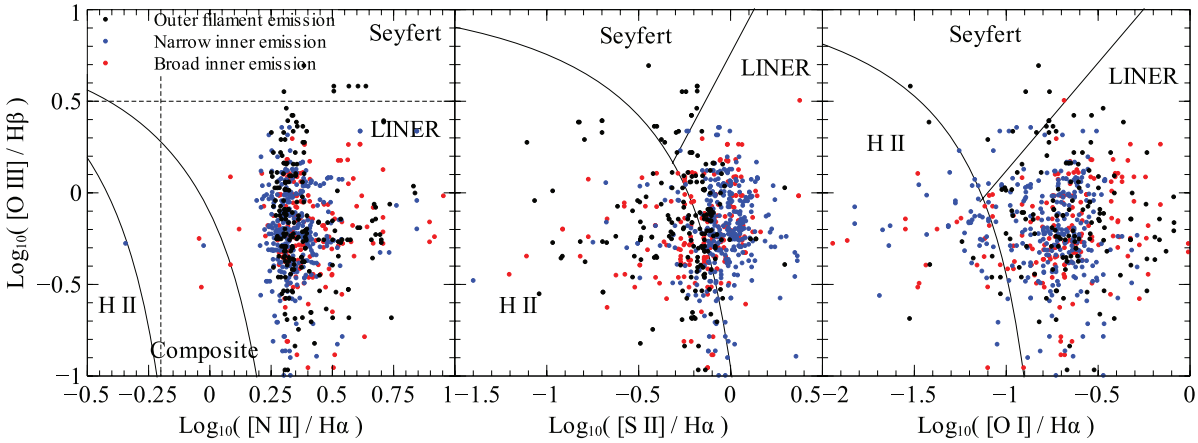

Figure 19. Ionization plots (Baldwin, Phillips & Terlevich 1981) of the outer and inner regions in the central 27 arcsec of NGC 4696. Left-hand panel: [O III] λ5007/Hβ λ4861 versus [N II] λ6583/Hα λ6563 emission. Middle panel: [O III] λ5007/Hβ λ4861 versus [O I] λ6300/Hα λ6563 emission. Right-hand panel: [O III] λ5007/Hβ λ4861 versus [S II] (λ6716 + λ6731)/Hα λ6563 emission. Solid lines are from Kewley et al. (2006) and dashed lines from Osterbrock & Ferland (2006).

velocity dispersions which show little variation across the whole length of some filaments.

3.8 Emission-line ratios

The emission-line ratios in the optical nebulosity are important tracers of the excitation processes dominating their behaviour. Heckman et al. (1989) suggested there was a bimodal population of BCGs based on their [N II]/Hα values and Hα luminosity. However, using a much larger cluster sample, Crawford et al. (1999) have shown that this is in fact a continuous spectrum with all objects sharing the characteristic low-ionization emission-line spectrum.

In a study by Wilman, Edge & Swinbank (2006) of four high-Hα-luminosity BCGs all situated in cool-core clusters and with the same LINER emission properties, the authors found no evidence for variations in line ratios as a function of either position or Hα luminosity across the galaxies. They interpret this as evidence for both a single ionization source for the line emission across each galaxy and a single dominant excitation mechanism in all of their galaxies. Hatch, Crawford & Fabian (2007) found, in a similar study of optical nebulosities surrounding six BCGs spanning a range of optical, X-ray and radio properties, that the ionization state of the optical nebulosities was not uniform and so concluded the converse, that is, a single scenario cannot be responsible for the optical-line emission in their sample. A recent study by Edwards et al. (2009) of further nine clusters, including in their sample both cool- and non-cool-core clusters, found diverse emission-line ratios and morphologies. This supports the finding by Hatch et al. (2007) that there is no one clear consistent mechanism to explain the origin of the line emission or to separate BCGs in cool- and non-cool-core clusters. Despite this there are some clear similarities in that a relatively hard-ionizing source is needed and that the systems are always well described by a LINER-like emission-line spectrum.

Hatch et al. (2006) studied in detail the spectral features in NGC 1275, a similar object in the centre of the Perseus cluster, and found radial variations in the [N II]/Hα emission-line ratio along the filaments with the inner regions having higher [N II]/Hα values. This could be due to an extra energy source closer in causing more heating per hydrogen ionization or due to metallicity variations in the filaments. Sarzi et al. (2006) also found variations in values of [O II]/Hβ along the length of the filaments in M87, the central galaxy in the Virgo cluster.

Maps of our emission-line ratios, binned using the contour binning algorithm of Sanders (2006), are shown in Fig. B2. The top panel shows the single Gaussian fits, the middle panel shows the broad central velocity component and the bottom panel in each case shows the narrow component. Only pixels where the line emission is detected at greater than 4σ are shown. An ionization plot (Baldwin et al. 1981) of the same pixels is shown in Fig. 19. The black points indicate the pixels where one emission-line component was found sufficient to model the emission lines, red points correspond to the broad lines and blue to the narrow. The [O III]/Hβ ratios cannot be traced across the whole length of the outer filaments as our HRB data cover only the central 27 arcsec and as such we cannot plot the most extended parts of the outer filaments in Fig. 19.

The scatter in Fig. 19 is large; however, NGC 4696 clearly exhibits LINER-like emission in both the central and extended regions. The broad inner component has in general a higher [N II]/Hα ratio than the narrow or outer regions, which are virtually indistinguishable from each other. If the broad component is from more centrally located emission, then this is consistent with the observation of Hatch et al. (2006) in NGC 1275 that [N II]/Hα ratios are in general higher towards the centre of the galaxy. If the filaments are shock-excited, we should see a gradient in emission-line ratios with velocity dispersion of the gas. Fig. 20 shows this ratio for the same three regions as in Fig. 19. No correlation is seen in the [N II]/Hα ratio with velocity width with most outer filaments (black points) having FWHM velocity widths of 100–200 km s^{-1} but ratios which vary from 1.8 to 3.3. We now examine the variation in emission-line ratios across the outer filaments in more detail by binning the emission in 3 × 3 arcsec^2 regions across the field of view (see Fig. 21).

3.9 Outer filaments

The north-west and southern filaments show a difference in the [N II] λ6583/Hα λ6563 emission ratios across their projected length with the southern filament decreasing and the north-western filament increasing in [N II] λ6583/Hα ratio (see Figs 21 and 22). The innermost regions of both filaments have a ratio ∼2, the average ratio of the galaxy. This difference in variation is in contrast to that seen in the filaments of NGC 1275 by Hatch et al. (2006) where

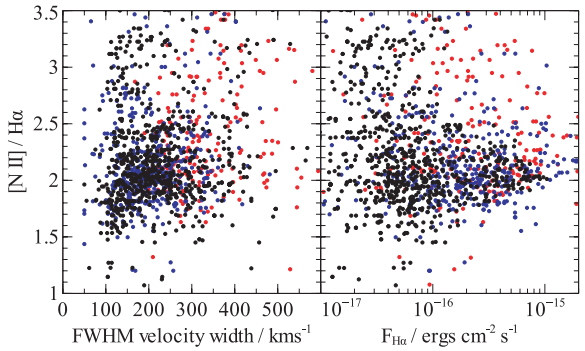

Figure 20. [N II] λ6583/Hα λ6563 ratio plotted against the FWHM velocity of each pixel and against the Hα flux. Only pixels where both [N II] λ6583 and Hα λ6563 were detected at the 4σ level are plotted. Colour-coding is the same as in Fig. 19.

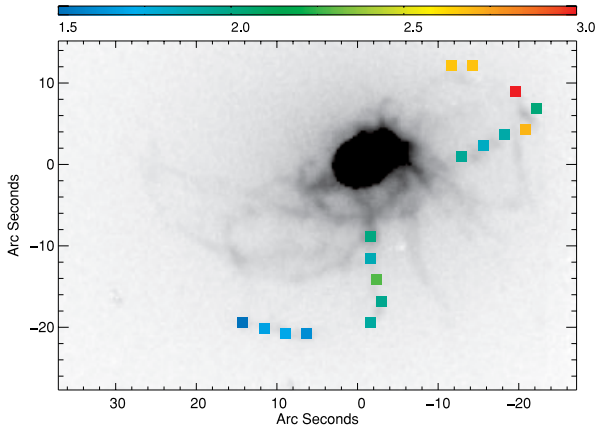

Figure 21. [N II] λ6583/Hα λ6563 emission ratios in the outer north-west and southern filaments. The emission is binned in 3 × 3 arcsec^2 regions across these filaments. Only regions where both emission lines were detected at greater than 4σ are shown.

there is a clear radial trend in [N II] λ6583/Hα intensity ratio seen in all long slits, with the ratio decreasing with projected distance from the nucleus.

A higher [N II] λ6583/Hα intensity ratio indicates that there is more heating occurring in the gas per hydrogen ionization. The difference in emission-line ratios in these two filaments could be due to the proximity of the filaments to the expanding radio bubble. The arm of the north-western filament appears to encircle the radio bubble, while the southern filament appears spatially less connected with the current radio emission.

The [N II] λ6583/Hα intensity ratio is also sensitive to variations in the metallicity of the gas. X-ray observations of the Centaurus cluster (Sanders et al. 2008) have shown that there is a high abundance of nitrogen emission in the central regions. Oxygen is an efficient coolant and high oxygen abundances in the gas would act to decrease the gas temperature and so reduce the observed [N II] λ6583/Hα ratio; however, the nitrogen/oxygen ratio in the hot gas is also high. The bottom panel of Fig. 22 shows the trend in [N II] λ6583/[O I] λ6300 emission-line ratios in the same filaments. There is weak evidence for a decreasing trend in [N II] λ6583/[O I] λ6300 ratio in these filaments.

The variation in the [N II] λ6583/Hα emission-line ratio with FWHM velocity width of the gas, in these two outer filaments, is shown in Fig. 23. There is no correlation between the measured

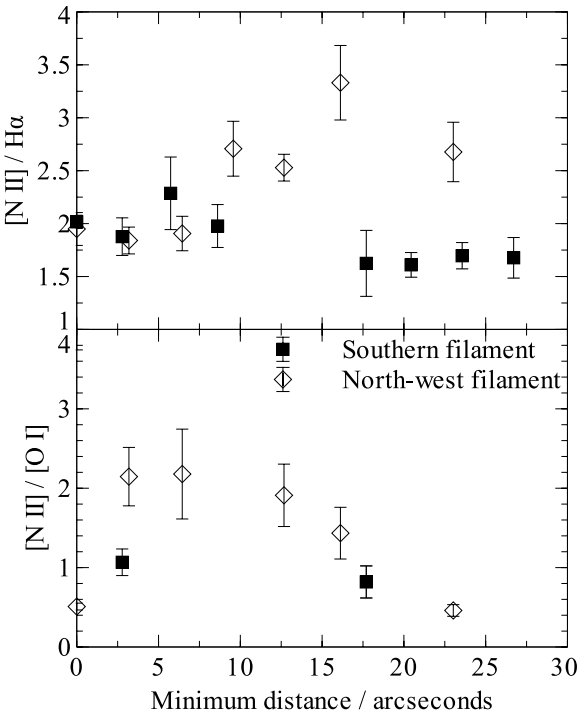

Figure 22. Variation in emission-line ratios as a function of projected distance along the north-west and southern filaments. Regions where spectra were extracted are shown in Fig. 21.

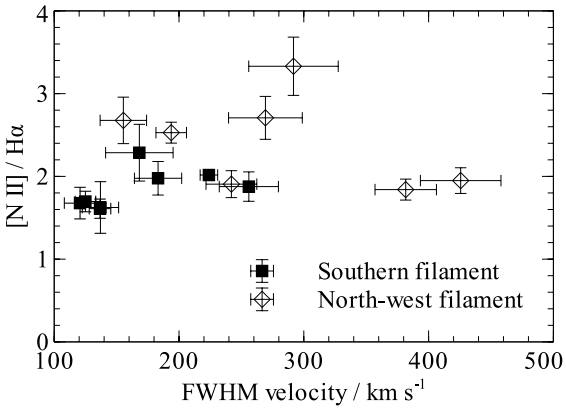

Figure 23. [N II] λ6583/Hα λ6563 emission ratio as a function of FWHM velocity width in the north-west and southern filament regions.

ratios and the width of the lines in either of the southern or north-western filaments. The majority of the emission has velocity widths less than 250 km s^{-1} and an emission-line ratio of ∼1.8–2.5. The two very broad regions in the north-west filament correspond to bright knots of emission which could be formed by the intersection of two or more individual filaments which cannot be resolved in our data.

4 CONCLUSIONS

The origin and excitation of the complex extended emission-line nebulae in BCGs and more specifically in NGC 4696 have been a matter of some controversy. Fig. 4 shows the close correspondence between the dust absorption and the [N II] emission tracing the 10^4 K emission-line nebula in NGC 4696. Virtually all extended filaments are spatially coincident with dust emission. Sparks et al.

(1989) do not find any deviation in the dust-extinction behaviour with wavelength with respect to dust within our Galaxy; similar results have been found in other BCGs. The authors suggest that this favours a merger origin for the emission-line filaments over the formation of the filament system straight from the hot gas.

There is, however, a third possibility that the gas originated due to dusty star formation in asymptotic giant branch atmospheres in the BCG and has been drawn out, rather than falling in, by buoyantly rising radio bubbles inflated by the AGN (Crawford et al. 2005). This scenario is supported by *Chandra* X-ray observations that reveal pressure minima towards the north-east at the end of the soft X-ray filaments and another minimum towards the south-west. These minima coincide with the outer edge of the 330-MHz radio emission and appear to be surrounded by regions of higher metallicity X-ray gas (Fabian et al. 2005).

Our deep optical IFU data allow us to explore in detail the morphology, kinematics and ionization properties of the optical nebulosity surrounding NGC 4696. We conclude the following:

(i) There are at least two velocity components to the emission-line gas in the inner regions of the galaxy. We interpret these as 'broader' and 'narrower' velocity width components.

(ii) These components have a different morphology, with the narrow component having a less smooth morphology and a striking bar of bright emission, while the broad component exhibits two peaks in emission, one peak coincident with the radio core and the other 4 arcsec to the west (see Fig. 9).

(iii) The peak in [O III] emission is spatially coincident with the nucleus and is offset from the brightest peak in [N II] emission (see Fig. 10).

(iv) The kinematics and emission-line spectra of the extended filaments are similar to those of filaments surrounding other BCGs.

(v) We do not find any evidence to suggest there is a correlation between the velocity width and [N II]/Hα ratio in the filaments of NGC 4696.

(vi) There is very little [O III] emission in the outer filaments as observed in similar systems.

The central 12 arcsec radius in NGC 4696 contains at least two components to the emission-line gas; we interpret these as a broad velocity component and a narrower component. The reddening and kinematical properties of the second component lead us to suggest it is a filament with properties much like the other extended filaments, which is located behind the main galaxy and thus more obscured by the intervening dust lanes. The morphology of the central region was previously thought to be a simple one-sided spiral structure perhaps caused by the tail of an infalling galaxy (Sparks et al. 1989; Farage et al. 2010); however, the filament system is clearly complex and it is not immediately obvious how a merger could account for the diversity in morphology of the filaments.

We find smoothly varying line-of-sight velocities in the outer filaments and low velocity widths (FWHM 50–250 km s^{-1}), with little variation along the length of many filaments, similar to those found in NGC 1275, the BCG in the Perseus cluster (Hatch et al. 2006). This is consistent with an origin for the filamentary system being slowly drawn up under the rising radio bubbles.

The spectrum of NGC 4696 exhibits the same strong low-ionization emission lines seen in many other extended emission-line systems surrounding BCGs. These systems are not all consistent with a merger origin. Johnstone et al. (2007) detected strong [Ne III] λ15.56 μm emission in their *Spitzer* IRS SH spectroscopy of NGC 4696 and 1275. Optical [Ne III] line emission has also been seen both in NGC 1275 (Hatch et al. 2006) and, weakly, in NGC 4696 (Farage et al. 2010). However, [O III] emission tends to be low in the extended emission-line systems in BCGs (e.g. Donahue et al. 2000). Johnstone et al. (2007) have shown that stellar photoionization models struggle to account for the high [Ne III] and low [O III] emission unless coupled with high metallicities. X-ray metallicities of typically solar for oxygen and neon (Sanders & Fabian 2006) are found in the centre of the Centaurus cluster and there is little sign of young stellar populations in the filaments.

The [O III] λ5007/Hβ emission in NGC 4696 drops dramatically from the nucleus to $\sim$12 arcsec, indicating the [O III] emission is low in the filaments and the majority of emission in the inner regions is associated with the nucleus. A similar trend is seen in many other BCGs (e.g. Johnstone & Fabian 1988). Our HRB data do not extend beyond the inner filament, so we cannot measure the [O III] emission in the farthest filaments from the nucleus. The ratio of our detected [O III] lines is small compared to shock models and the upper limit of the weak [O III] λ4364 line indicates an [O III] λ4364/Hβ ratio of 5 per cent, lower than the predicted value from the best velocity shock model of Farage et al. (2010).

Ferland et al. (2008, 2009) have shown that the characteristic LINER spectrum with anomalously low [O III] and high [Ne II] and [Ne III] emission, compared to photoionization models, can be reproduced with their particle heating model. With the exception of [N II] λ6583, which is underpredicted, all our optical emission lines detected in the outer filaments in NCG 4696 are within a factor of 2 or less of their predicted spectrum. The predicted spectrum of Ferland et al. (2009) uses a gas-phase abundance of nitrogen relative to hydrogen of 6.9×10^{-5} which corresponds to $\sim$0.5 $Z_{\odot}$ using abundances from Anders & Grevesse (1989). Sanders et al. (2008) find the nitrogen abundance in Centaurus to be approximately four times solar in the central regions, a factor of 8 times that used in the predicted particle heating spectrum. The predicted emission-line ratios do not in general behave linearly with changes in metallicity of the gas due to the thermostat effect, where increasing the abundance of a coolant lowers the kinetic temperature to conserve energy (Osterbrock & Ferland 2006). However, the emissivities of [N II] and Hα are predicted to be relatively constant over a broad range of temperatures ($10^{3.8}$–$10^{4.4}$ K) within the thermally stable regime (see fig. 17 of Ferland et al. 2009) so an increase in the nitrogen abundance by 8 would result in an increase in the [N II]/Hα ratio. Note though that this is not necessarily the case for the [N I] emission which does not exhibit such a flat emissivity profile. Future papers will explore the effect of varying metallicity on the particle heating model ratios.

ACKNOWLEDGMENTS

REAC acknowledges the STFC for financial support. ACF thanks the Royal Society. REAC would also like to thank Ryan Cooke, Bob Carswell and Paul Hewett for interesting and enlightening discussions.

This research has made use of the NASA/IPAC Extragalactic Database, which is operated by the Jet Propulsion Laboratory, California Institute of Technology, under contract with the National Aeronautics and Space Administration.

REFERENCES

Amico P., Bagnulo S., Dumas C., Izzo C., Marconi G., Melo C., 2008, in Kaufer A., Kerber F., eds, Proc. ESO Workshop, The 2007 ESO Instrument Calibration Workshop. Springer, Berlin, p. 279

Anders E., Grevesse N., 1989, Geochim. Cosmochim. Acta, 53, 197

Baldwin J. A., Phillips M. M., Terlevich R., 1981, PASP, 93, 5

Bohringer H., Nulsen P. E. J., Braun R., Fabian A. C., 1995, MNRAS, 274, L67
Bruzual G., Charlot S., 2003, MNRAS, 344, 1000 (BC03)
Calzetti D., Armus L., Bohlin R. C., Kinney A. L., Koornneef J., Storchi-Bergmann T., 2000, ApJ, 533, 682
Canning R. E. A., Fabian A. C., Johnstone R. M., Sanders J. S., Crawford C. S., Hatch N. A., Ferland G. J., 2011, MNRAS, 411, 411
Cappellari M., Copin Y., 2003, MNRAS, 342, 345
Churazov E., Brüggen M., Kaiser C. R., Böhringer H., Forman W., 2001, ApJ, 554, 261
Cid Fernandes R., Mateus A., Sodré L., Stasińska G., Gomes J. M., 2005, MNRAS, 358, 363
Cid Fernandes R., Jarvis M. J., Rawlings S., 2009, Rev. Mex. Astron. Astrofís. Ser. Conf., 35, 127
Cowie L. L., Fabian A. C., Nulsen P. E. J., 1980, MNRAS, 191, 399
Crawford C. S., Fabian A. C., 1992, MNRAS, 259, 265
Crawford C. S., Allen S. W., Ebeling H., Edge A. C., Fabian A. C., 1999, MNRAS, 306, 857
Crawford C. S., Hatch N. A., Fabian A. C., Sanders J. S., 2005, MNRAS, 363, 216
Donahue M., Stocke J. T., Gioia I. M., 1992, ApJ, 385, 49
Donahue M., Mack J., Voit G. M., Sparks W., Elston R., Maloney P. R., 2000, ApJ, 545, 670
Edge A. C., 2001, MNRAS, 328, 762
Edge A. C., Wilman R. J., Johnstone R. M., Crawford C. S., Fabian A. C., Allen S. W., 2002, MNRAS, 337, 49
Edwards L. O. V., Robert C., Mollá M., McGee S. L., 2009, MNRAS, 396, 1953
Fabian A. C., Nulsen P. E. J., Canizares C. R., 1984, Nat, 310, 733
Fabian A. C., Sanders J. S., Crawford C. S., Conselice C. J., Gallagher J. S., Wyse R. F. G., 2003, MNRAS, 344, L48
Fabian A. C., Sanders J. S., Taylor G. B., Allen S. W., 2005, MNRAS, 360, L20
Fabian A. C., Johnstone R. M., Sanders J. S., Conselice C. J., Crawford C. S., Gallagher J. S., III, Zweibel E., 2008, Nat, 454, 968
Farage C. L., McGregor P. J., Dopita M. A., Bicknell G. V., 2010, ApJ, 724, 267
Ferland G. J., Korista K. T., Verner D. A., Ferguson J. W., Kingdon J. B., Verner E. M., 1998, PASP, 110, 761
Ferland G. J., Fabian A. C., Hatch N. A., Johnstone R. M., Porter R. L., van Hoof P. A. M., Williams R. J. R., 2008, MNRAS, 386, L72
Ferland G. J., Fabian A. C., Hatch N. A., Johnstone R. M., Porter R. L., van Hoof P. A. M., Williams R. J. R., 2009, MNRAS, 392, 1475
Hatch N. A., Crawford C. S., Johnstone R. M., Fabian A. C., 2006, MNRAS, 367, 433
Hatch N. A., Crawford C. S., Fabian A. C., 2007, MNRAS, 380, 33
Heckman T. M., Baum S. A., van Breugel W. J. M., McCarthy P., 1989, ApJ, 338, 48
Hu E. M., Cowie L. L., Wang Z., 1985, ApJS, 59, 447
Jaffe W., Bremer M. N., van der Werf P. P., 2001, MNRAS, 324, 443
Johnstone R. M., Fabian A. C., 1988, MNRAS, 233, 581
Johnstone R. M., Fabian A. C., Nulsen P. E. J., 1987, MNRAS, 224, 75
Johnstone R. M., Hatch N. A., Ferland G. J., Fabian A. C., Crawford C. S., Wilman R. J., 2007, MNRAS, 382, 1246
Jorgensen H. E., Norgaard-Nielsen H. U., Pedersen H., Rasmussen I. L., Schnopper H., 1983, A&A, 122, 301
Kent S. M., Sargent W. L. W., 1979, ApJ, 230, 667
Kewley L. J., Groves B., Kauffmann G., Heckman T., 2006, MNRAS, 372, 961
LeFevre O. et al., 2003, in Iye M., Moorwood A. F. M., eds, SPIE Conf. Ser. Vol. 4841, Instrument Design and Performance for Optical/Infrared Ground-based Telescopes. SPIE, Bellingham, p. 1670
McNamara B. R., Nulsen P. E. J., 2007, ARA&A, 45, 117
McNamara B. R., O'Connell R. W., Sarazin C. L., 1996, AJ, 112, 91
Markwardt C. B., 2009, in Bohlender D. A., Durand D., Dowler P., eds, ASP Conf. Ser. Vol. 411, Astronomical Data Analysis Software and Systems XVIII. Astron. Soc. Pac., San Francisco, p. 251
Moré J. J., 1978, The Levenberg-Marquardt Algorithm: Implementation and Theory. Springer-Verlag, Berlin
Osterbrock D. E., Ferland G. J., 2006, Astrophysics of Gaseous Nebulae and Active Galactic Nuclei, 2nd edn. University Science Books, Mill Valley, CA
Peterson J. R., Fabian A. C., 2006, Phys. Rep., 427, 1
Postman M., Lauer T. R., 1995, ApJ, 440, 28
Reynolds C. S., McKernan B., Fabian A. C., Stone J. M., Vernaleo J. C., 2005, MNRAS, 357, 242
Sabra B. M., Shields J. C., Filippenko A. V., 2000, ApJ, 545, 157
Salomé P., Combes F., 2003, A&A, 412, 657
Sanders J. S., 2006, MNRAS, 371, 829
Sanders J. S., Fabian A. C., 2002, MNRAS, 331, 273
Sanders J. S., Fabian A. C., 2006, MNRAS, 371, 1483
Sanders J. S., Fabian A. C., Allen S. W., Morris R. G., Graham J., Johnstone R. M., 2008, MNRAS, 385, 1186
Sarzi M. et al., 2006, MNRAS, 366, 1151
Scodeggio M. et al., 2005, PASP, 117, 1284
Sparks W. B., Macchetto F., Golombek D., 1989, ApJ, 345, 153
Taylor G. B., Fabian A. C., Allen S. W., 2002, MNRAS, 334, 769
Terlevich R., Melnick J., 1985, MNRAS, 213, 841
Veilleux S., Osterbrock D. E., 1987, ApJS, 63, 295
Voit G. M., Donahue M., 1997, ApJ, 486, 242
Wilman R. J., Edge A. C., Swinbank A. M., 2006, MNRAS, 371, 93
Zanichelli A. et al., 2005, PASP, 117, 1271

APPENDIX A: DATA-REDUCTION PLOTS

A1 Sky absorption and emission corrections

The VIMOS IFU does not have dedicated sky fibres and unlike slit spectroscopy an individual spectrum on a fibre does not have

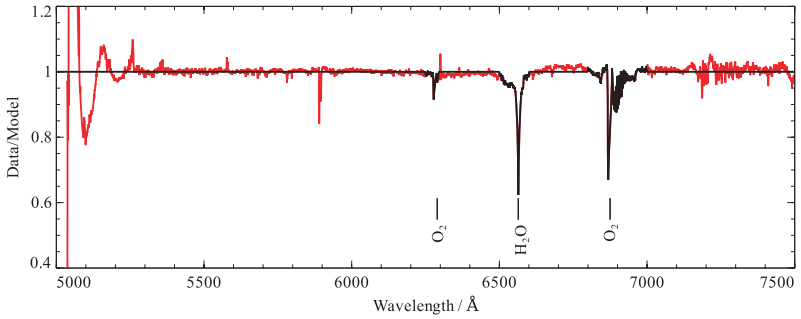

Figure A1. Telluric absorption correction for Q1 using four standard star observations. We only correct for atmospheric absorption between 5500 and 7000 Å. The absorption seen at ∼5900 Å is likely NaD absorption from our Galaxy and as such has not been corrected for. The red line shows the median observed spectrum of the four standard stars divided by their intrinsic spectrum. The black line is the telluric correction we apply to our data.

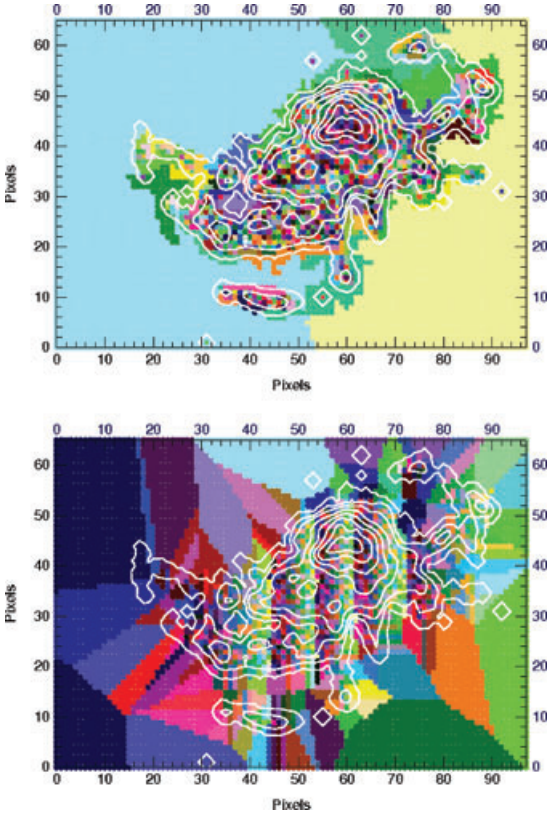

Figure A2. Top panel: the contour binning algorithm of Sanders (2006) applied to a 2D brightness map of [N II] λ6583 emission in NGC 4696. Bottom panel: the same using the Veronoi tessellation binning algorithm of Cappellari & Copin (2003). Both maps show the data binned to a signal-to-noise ratio of 10.

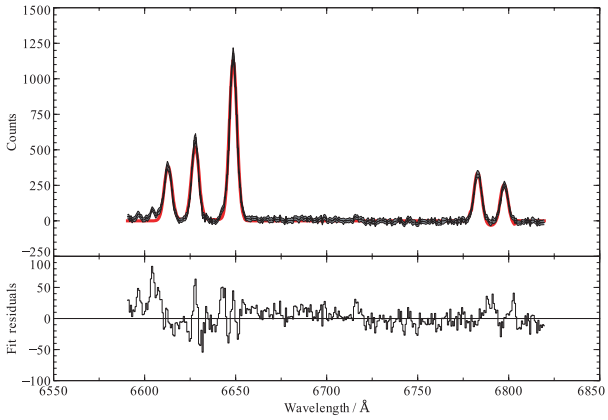

Figure A5. An example single Gaussian fit to the strongest emission lines in our spectra. These are the lines of [N II] λ6548, Hα λ6563, [N II] λ6583, [S II] λ6717 and [S II] λ6730. These lines are fitted between 6590 and 6820 Å. A fixed continuum has been subtracted and is estimated as the median value between 6700 and 6750 Å. The continuum regions around the Hα+[N II] doublet and the [S II] doublet are fitted separately. The data and error are shown as a thick grey line, the red line indicates the model fit to the data and the fit residuals are shown in the bottom panel.

both regions with pure sky emission and regions with object and sky emission. Different fibre spectra are described by different profile shape parameters such as the FWHM and skewness. In the wavelength direction, this results in the spectral lines having different shapes and thus affects the quality of the sky subtraction. An average sky spectrum formed by combining spectra with different line profiles can result in the presence of s-shape residuals when subtracted from the data. VIPGI sky subtraction attempts to correct for these line profiles by grouping the spectra

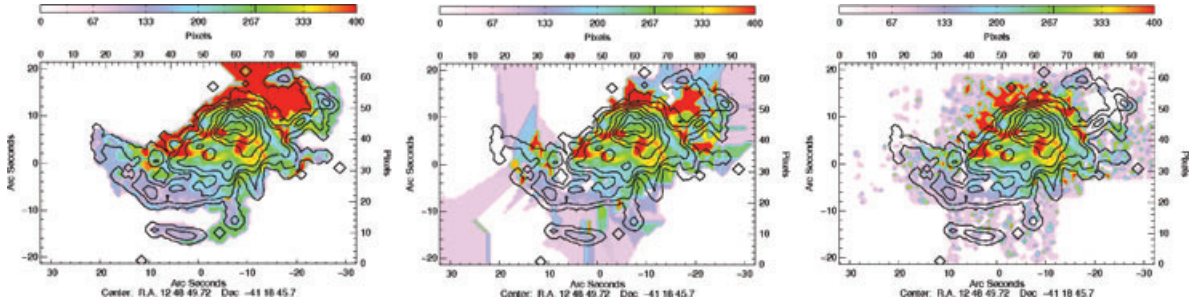

Figure A3. FWHM velocity dispersion, in units of km s^{-1}, for different binning techniques for a single Gaussian fit to the [N II], Hα and [S II] lines. Left-hand panel: binning to a signal-to-noise ratio of 10 using the contour binning technique of Sanders (2006). Middle panel: binning to a signal-to-noise ratio of 10 using the Veronoi tessellation technique of Cappellari & Copin (2003). Right-hand panel: the velocity dispersion on a per pixel basis across the field of view. Here the (0,0) position corresponds to the centre of the image.

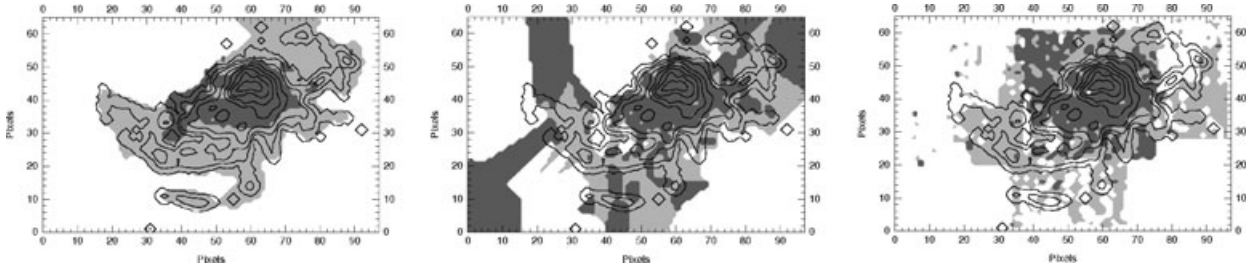

Figure A4. Regions where the fibres are statistically found to be described by one or two velocity components for the spectra binned by surface brightness (left-hand panel), Voronoi binning (middle panel) and no-binning (right-hand panel). The darker shade indicates two components were necessary to fit the spectra. Regions in a lighter shade were found to be modelled sufficiently with a single velocity component.

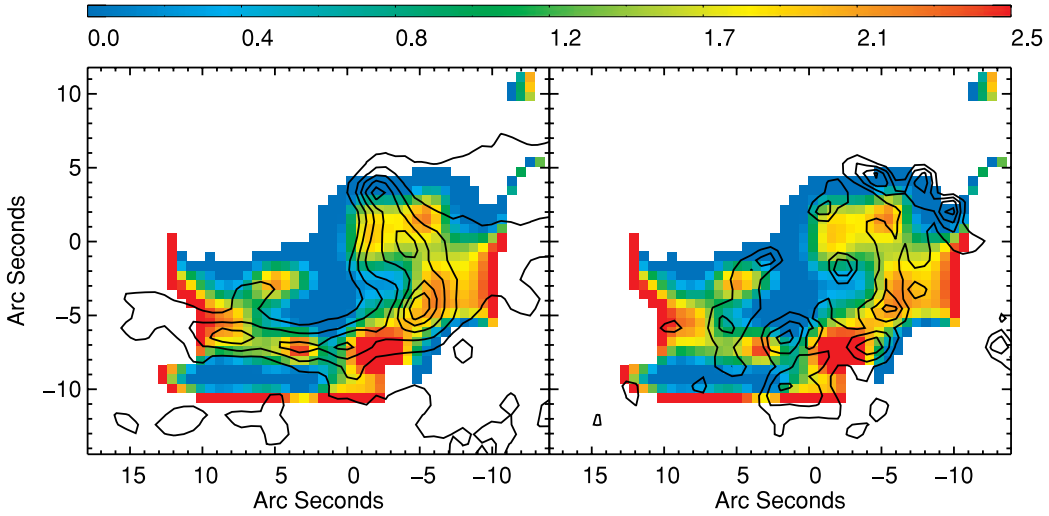

Figure B1. A_V intrinsic extinction maps derived from the Hα/Hβ ratio, fitted with a single Gaussian. Left-hand panel: overlaid with contours of $E(B-V)$. Right-hand panel: overlaid with contours of X-ray $N_{\rm H}$. Contours are from Crawford et al. (2005). The colour bar shows the intrinsic A_V extinction calculated assuming a case B intrinsic recombination ratio (Osterbrock & Ferland 2006); only pixels where both Hα and Hβ were detected at 4σ or above are shown; the original fits were smoothed by a Gaussian with FWHM 3 pixels (2 arcsec).

according to a user-defined skyline. An average sky for each spectrum grouping is then calculated and subtracted. The groupings are done on a statistical basis; thus, this sky-subtraction method employed by the VIPGI is optimized for deep survey observations where the field is devoid of extended objects. It is not ideal for observing large galaxies which dominate the field of view. For this reason, we performed the sky subtraction using specific fibres shown to be lacking in emission lines associated with NGC 4696.

Telluric absorption feature corrections for the O_2 and H_2O absorption in the 6000–7000 Å band was determined from four observations of standard stars. Standard stars were observed at the beginning and the end of the night. The stars chosen are CD-32-9927, LTT-7379, Hiltner-600 and LTT-2415. The standard spectra $G(\lambda)$ were reduced using the VIPGI, as with the science observations. These spectra were divided by the ESO spectra $G_0(\lambda)$ of the respective standards, corrected for atmospheric absorption. These observations were then averaged for each VIMOS IFU quadrant and the area around the absorption lines was isolated. Fig. A1 shows the Q1 spectra of each of the four standard stars and the averaged normalized spectrum.

Ignoring the curvature of the Earth, we recover the object spectrum as seen without the atmospheric absorption (F_0),

$$F_0(\lambda) = F(\lambda)\left[\frac{G_0(\lambda)}{G(\lambda)}\right]^{\frac{X_{\rm object}}{X_{\rm standard}}}, \tag{A1}$$

for each 15 min exposure separately so as to correct for airmass differences between the standard star ($X_{\rm standard}$) and the object ($X_{\rm object}$).

A2 Propagation of uncertainties

Our HRO and HRB spectra overlap between 5000–6000 Å. In order to incorporate all our data, we split the cubes into three wavelength regions. The regions chosen are 4000–5100, 5100–5800 and 5800–7500 Å. The two HR grisms used have a slightly different spectral resolution (see Table 1) with the resolution of the HRO grism being marginally larger than that of the HRB grism. In order to amalgamate both data sets, it is necessary to re-bin the HRO spectra. If we are re-binning original bins i into bins j where some fraction w_{ij} of i falls into the jth bin, then we determine the flux F_j and error S_j in the jth bin by

$$F_j \pm S_j = \sum_i w_{ij} f_i \pm \sqrt{\sum_i w_{ij} e_i^2}, \tag{A2}$$

where f_i is the flux in original bin i and e_i^2 is the variance in bin i. For pixel-to-pixel fluctuations, the error E_j is given by $E_j = \sqrt{\sum_i w_{ij}^2 e_i^2}$. The HRO and HRB spectra are then summed and the total flux $\mathcal{F}_j$ in the re-binned grid is given by (Bob Carswell, private communication[2])

$$\mathcal{F}_j = \frac{\sum_k \frac{F_j^k}{\left(S_j^2\right)^2}}{\sum_k \frac{1}{\left(S_j^k\right)^2}}, \tag{A3}$$

where k is the number of spectra summed together. The estimate of the fluctuations in the spectra is then given by

$$\mathcal{E}_j^2 = \frac{\sum_k \left[\frac{E_j^k}{\left(S_j^k\right)^2}\right]^2}{\left[\sum_k \frac{1}{\left(S_j^k\right)^2}\right]^2}. \tag{A4}$$

This forms the error spectrum used when fitting Gaussian models to the emission lines and minimizing the resulting χ^2.

A3 Spatial binning

To improve the signal-to-noise ratio in the spectra, we investigate the use of two spatial binning algorithms: that of Sanders (2006), which bins the data based on surface brightness, and that of Cappellari & Copin (2003), which uses Voronoi tessellations to provide the most 'round' bins. The two techniques applied to our NGC 4696 data are shown in Fig. A2.

[2] ftp://ftp.ast.cam.ac.uk/pub/rfc/vpfit9.5.pdf

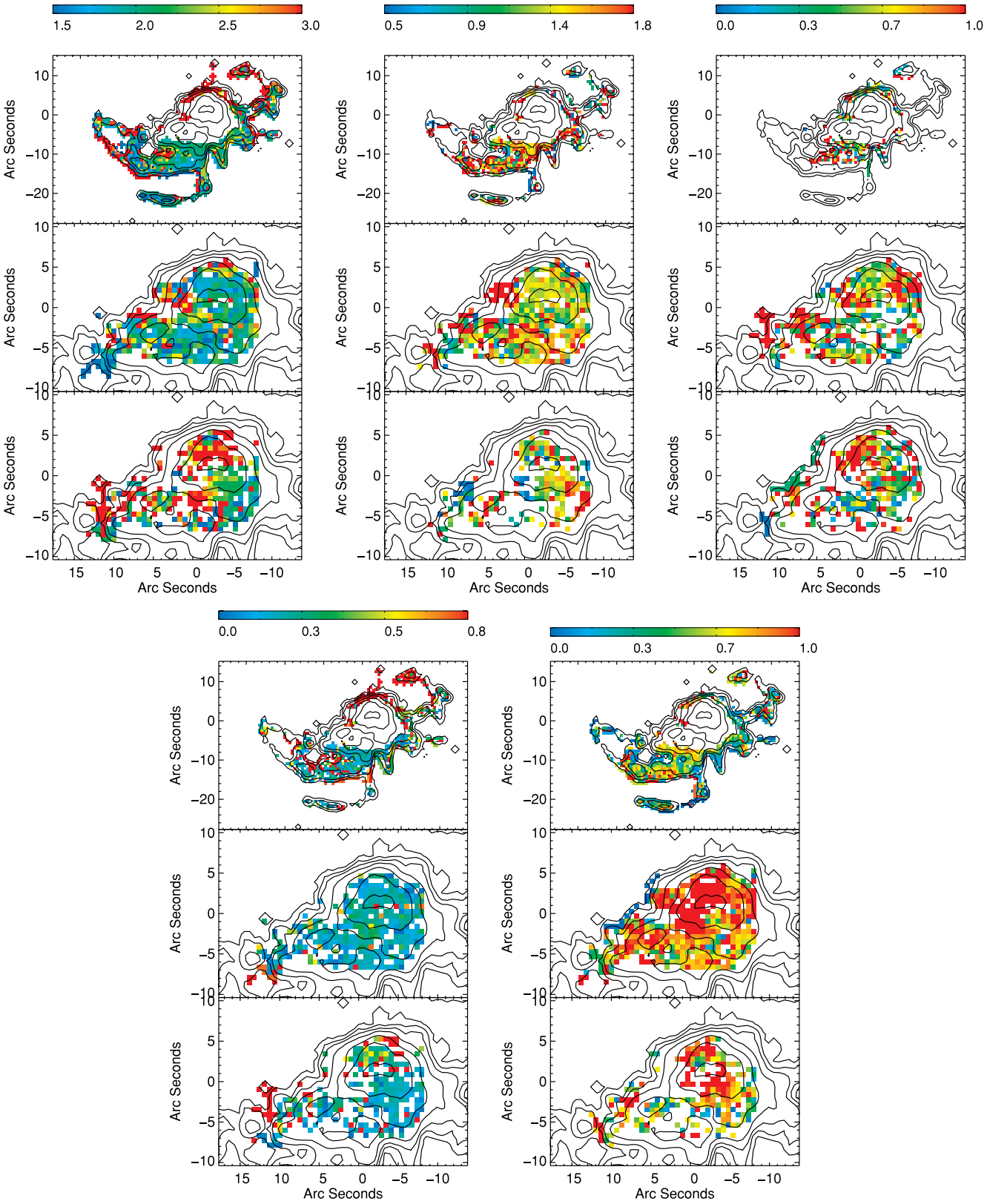

Figure B2. Clockwise from the top left-hand figure: [N II] λ6583/Hα λ6563, [S II] λ6716/[S II] λ6731, [O III] λ5007/Hβ λ4861, [S II] (λ6716 + λ6731)/Hα λ6563 and [O I] λ6300/Hα λ6563 emission. The top panel in each figure is the ratio in the outer filaments where only one velocity component was detected. The middle panel is the narrow component of the two-component Gaussian fit and the bottom panel is the broad component.

Both techniques give similar fits over comparable regions, giving us confidence that the physical properties of the regions we are binning are similar to the limit of our spatial resolution (see Fig. A3). Due to the filamentary structure of the optical-line nebulosity surrounding NGC 4696, we choose to bin our spectra using the contour binning technique of Sanders (2006).

A4 Velocity-component fitting

The data are fitted with multiple velocity components. An example single-velocity-component fit to the Hα, [N II] and [S II] emission lines is shown in Fig. A5. An F-test is then performed to determine whether extra velocity components are required.

The lower panels in Fig. A4 show the results of the F-test when the data are binned by surface brightness contour binning, Voronoi tessellations and no-binning. The darker shade implies two velocity components are necessary and the light shade indicates the spectra were sufficiently well represented with a single Gaussian velocity component.

APPENDIX B: EMISSION-LINE MAPS

The reddening map for a one velocity component fit, on a per pixel basis, in the central regions of NGC 4696 is shown in Fig. B1. Contours of $E(B-V)$ derived from *HST* *B*- and *I*-band images and *Chandra* X-ray $N_{\rm H}$ column density (Crawford et al. 2005) are overlaid.

Maps of our emission-line ratios, binned using the contour binning algorithm of Sanders (2006), are shown in Fig. B2. The top panel shows the single Gaussian fits, the middle panel shows the broad central velocity component and the bottom panel in each case shows the narrow component. Only pixels where the line emission is detected at greater than 4σ are shown. The [O III]]/Hβ ratios cannot be traced across the whole length of the outer filaments as our HRB data only cover the central 27 arcsec.

This paper has been typeset from a TEX/LATEX file prepared by the author.